Tampere University

Asha Basak

STACKABLE MODULAR 3D PRINTED BIOACTIVE GLASS SCAFFOLDS WITH METAL SCREWS

Master's Thesis
Faculty of Medicine and Health Technology
Jeffrey Anker
Jonathan Massera
March 2023

ABSTRACT

Asha Basak: Stackable modular 3D printed bioactive glass scaffolds with metal screws
Master's Thesis
Tampere University
Master's Degree Programme in Biotechnology and Biomedical Engineering
April 2023

Bioactive glass has been widely studied for its potential in various biomedical applications, particularly in the field of tissue engineering and regenerative medicine. The surface of bioactive glass can dissolve and precipitate a hydroxyapatite layer when it comes into contact with body fluids, which mimics the structure of natural bone and promotes bone growth. The main aim of this Master's Thesis is to develop a new approach to making bone replacement scaffolds which can meet the various demands of large bone scaffolds used to treat large defects usually induced from trauma or bone cancer. For example, mandible replacement is important because with an injured mandible daily essential works such as biting, chewing, speaking become very difficult. However, the replaced part needs mechanical properties shape, size, ability to tailor intraoperatively, bioactivity, perfusion, and ability to add sensors actuators. It is difficult for a single material to have all requisite properties in practice. To address these issues, we 3D printed porous bioactive glass scaffolds, stack them with the stainless steel screws after the sintering process.

As a proof of concept, a structure with modular components including large holes to fit metallic screws was produced, to take the load. The sintered hexagon scaffolds were stacked with stainless steel screws so that it makes them as strong as the trabecular or cortical bone. In order to stack the scaffolds, larger holes must be made in the scaffolds for the screws to fit. The main goal is to incorporate the bioactivity of the bioactive glass and mechanical strength of the stainless steel screws so that the scaffolds are not only bioactive, biocompatible but also have strong mechanical properties like human bone. The background related studies and motivation of the thesis were described in chapter one and chapter two of this thesis.

The B12.5 MgSr borosilicate glass and 25 wt% Pluronic was used for 3D printing of all shape of scaffolds including: hexagon, logpile and ordinary logpile. Two sintered hexagon scaffolds were stacked with the stainless steel screws and one titanium plate was added on the top, and one titanium plate on the bottom. Some small holes were created in the titanium plates to mimic the porous structure. The mechanical properties (load/displacement curves) for these stacked scaffolds analyzed with a mechanical testing stand and compared to scaffolds without metal. The detailed method for making ink, 3D printing and sintering of the scaffolds, stacking the scaffolds and measuring and analyzing the mechanical properties are described in chapter three.

We examined the mechanical properties of the scaffolds in terms of Young's modulus, maximum compressive strength and compressive strain at maximum compressive strength. The mean Young's modulus of the single hexagon sample was 2.4±1 MPa and for single logpile scaffolds was 1.5±0.7 MPa. While the stacked hexagon scaffold's mean Young's modulus was 122±33 MPa. This means that the stacking and adding metal plates and screws vastly increased the Young's Modulus. The maximum compressive strength of the logpile scaffolds were very low (0.02 MPa) as they bent into concave shapes after sintering which reduced the contact area of the scaffold and the plates of the Instron Electropuls compression platen. The mean maximum compressive strength of the hexagon scaffolds was 0.2±0.4 MPa where for the stacked hexagon scaffold it was 3.3±2 MPa. The Young's modulus and the maximum compressive strength of the trabecular bone are 50-500 MPa and 0.1-16 MPa. However, the ordinary logpile scaffolds had better result than stacked scaffolds as their Young's modulus and maximum compressive strength were 329±216 MPa and 4.8±3 MPa albeit over a smaller strain range. The ordinary scaffolds are less porous, smaller and more uniform than the hexagon and logpile scaffolds that we used. Overall, our results showed the metal screws does help increasing the mechanical properties of the stacked hexagon scaffolds as they have the Young's Modulus and maximum compressive strength similar to trabecular bone.

Keywords: Bioactive glass scaffold, Bone scaffold, 3D printing, Regenerative medicine, Young's Modulus, Maximum compressive strength.
The originality of this thesis has been checked using the Turnitin OriginalityCheck service.

PREFACE

I became interested in bone tissue engineering and bioactive during my Master's studies. So I wanted to do my thesis in this field. As a result, I contacted Jonathan Massera who is the Head of the Bioceramics, Bioglasses and Biocomposites group in Tampere University. Luckily, I got an interesting topic under the supervision of Jeffrey Anker and Jonathan Massera.

I am very thankful to Jeffrey Anker and Jonathan Massera to provide me this opportunity and to guide me throughout the thesis. I want to thank Tommi Salo, Petteri Niemela, Virginia Alessandra Gobbo and specially Agata Szczodra and Sonya Ghanavati for helping me in different stages of the project and cheering me up during the hard times. Lastly, I want to express my gratitude towards my family because without them I would not be able to make it this far.

Tampere, 14 April 2023

Asha Basak

TABLE OF CONTENTS

LIST OF FIGURES

LIST OF SYMBOLS AND ABBREVIATIONS

BTE	Bone tissue engineering
BMUs	Basic multicellular units
ECM	Extracellular matrix
BMP-2	Bone morphogenic protein-2
HA	Hydroxyapatite
ACP	Amorphous calcium phosphate
SBF	Simulated body fluid
mol%	Percentage by mole
µCT	Micro-computed tomography

.

1. INTRODUCTION

The enormous number of bone defects brought on by cancer, trauma continue to be a major concern for patients and doctors. The rate of bone growth depends on several factors, including bone size and anatomical location, mechanical stability, soft tissue envelope, metabolic factors, infection and others. When a bone defect is larger than a critical size, typically around 2-2.5x the bone diameter, it is unable to heal on their own [1].

To heal, the fracture needs to be pushed closer (reduced), or linked with another piece of bone or bone mimic. Bone regeneration is a complicated biological phenomenon, that provides the bones with a template that can be followed to heal the affected part of the bones. Nowadays bone regeneration techniques such as autografts and allografts can provide expected osteoconductivity, osteogenesis, and osteoinductivity [2].

An autograft is a surgical procedure in which a patient's own tissue is transplanted from one part of the body to another. In the context of bone grafting, an autograft involves taking a small piece of bone from a donor site in the patient's body, such as the hip or the ribs, and using it to fill a bone defect or promote bone healing in another area of the body. Autografts are preferred in many cases because they have several advantages over other types of bone grafts. Since the graft material is taken from the patient's own body, there is a reduced risk of rejection, infection, or disease transmission. Autografts also contain living cells and growth factors that promote bone healing, and they can integrate more readily with the surrounding bone tissue. However, harvesting an autograft can be a painful procedure, and it may also result in additional scarring or complications at the donor site. On the other hand, an allograft is a surgical procedure in which bone tissue is transplanted from a donor of the same species but different individual, usually from a cadaveric source, into a recipient's body to promote bone healing or replace missing or damaged bone. In the context of bone grafting, allografts can be used as an alternative to autografts, where the bone tissue is harvested from the patient's own body. However, allografts have some limitations, such as a higher risk of rejection compared to autografts, and a lower concentration of living cells and growth factors that promote bone regeneration. Furthermore, there is a small risk of disease transmission [3,4]. The allografts require additional preparation and cleaning processes that eliminate the

cells and reduce the risk of immune response but eventually decrease the mechanical strength, osteoinductivity, osteoconductivity of the graft [5].

Hence, bone tissue engineering (BTE) can be a potential method for the treatment of bone defects. 3D scaffolds microstructures can be used to replicate the host bones. Bioactive glasses are recently getting popular in the BTE research because they are osteoconductive and osteoinductive if properly made [6].

Bioactive glasses are materials that can bond with living tissues, promoting the growth of new bone and helping to repair damaged tissue. When bioactive glass is implanted in the body, it begins to interact with the body fluid. Then it generates an apatite that influences the new bone growth [7].

Among bioactive glasses, B12.5 MgSr borosilicate glass has low coefficient of thermal expansion, making it highly resistance to thermal shock and suitable for applications where dimensional ability is important. The 3D printed scaffolds need to be biocompatible, porous and have a high degree of accuracy to mimic the natural structure if the tissue. Notably, B12.5 MgSr borosilicate glass can be sintered without significant crystallization which enables the creation of highly porous structure with controlled pore sizes and shapes [8].

The effectiveness of scaffolds depends on a delicate balance of chemical/biological characteristics of materials and production processes. The bioactivity, osteogenic potential, dissolution rates depend on how properly the scaffolds are made. Sintering is an important step in the manufacturing process of bioactive glass scaffolds, as it can improve their mechanical properties, tailor their porosity, enhance their bioactivity, and improve their biocompatibility, all of which are critical for successful tissue engineering applications [9].

We are trying to robocast a bone scaffold that will maintain the porosity of bone and can enhance bone growth. As they would be made of bioactive glass, they would dissolve and produce ions that will help in bone and vascular growth in the scaffold. In most of the studies, the used 3D scaffolds look like Figure 1.1 which is a logpile scaffold. The scaffolds internally and externally designed in such a way so that they can provide the appropriate environment and architecture for developing tissue. They are provisional matrices through which bones are formed [10,11]. The scaffolds provide the environment so that cellular allocation, differentiation and growth are influenced. The pores are an important factor in designing scaffolds. The scaffolds need to be porous and the pores need to be opened. Capillary ingrowth and cell-matrix connections require microporosity

having pores smaller than 10 μm. Macroporosity with pore diameters ranging from 150 to 900 μm enables nutrition delivery and waste disposal of cells reproducing on the scaffold [12, 13]. As a result, optimal porosity is required to have better permeability, nutrients supply, etc. In most of the studies grid like layers (see Figure 1.1) are designed. However, the downfalls of using bioactive glass scaffolds are, they are fragile and their fracture toughness is small. Correspondingly, they cannot be used in the load bearing implants [14-17]. Hence, major bone damage healing and renewal at load-bearing anatomical locations remains a clinical problem [18].

To solve this issue, we tried to add stainless steel screws to the scaffolds by stacking the scaffolds with screws. To fit the screws in the scaffolds, the scaffolds require bigger holes in them. We designed the scaffolds having each layer looks like Figure 1.2. The reason is, we want the holes to be bigger so that we can stack at least two scaffold with metal screws.

Figure 1. 1. *Photograph of two gridded sintered logpile scaffolds (size: 5.7mm x5.7mm x5mm)*

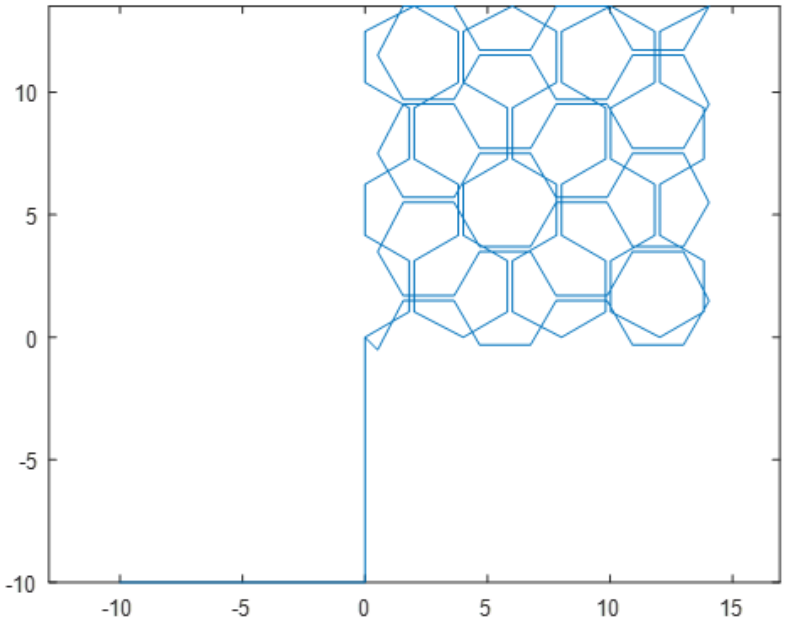

Figure 1. 2. *Position of robocastor for the layers of the hexagon scaffolds. Scale is in millimeters.*

The logic behind using metal screws in the scaffolds is we want the bioactive properties of the bioactive glass scaffolds as well as mechanical strength of the stainless steel. The main idea is to create the scaffold having mechanical properties (Young's modulus, Compressive strength, etc.) similar to the Trabecular bone or cortical bone. The mechanical properties of Trabecular and cortical bones are shown in Table 1.1. We described the structure and properties of bone below in chapter 2.

Table 1.1. *Mechanical properties of human trabecular and cortical bone [19]*

Material property	Trabecular bone	Cortical bone
Compressive strength [MPa]	0.1–16	130–200
Young's modulus [GPa]	0.05–0.5	7–30

2. BACKGROUND

2.1. Bone Tissue Engineering

2.1.1. Structure of Bone

Human bone has always been the subject of interest in the material engineering field as it has special mechanical properties. Bones are responsible for supporting and protecting the body's internal organs, providing a framework for muscles to attach and move, and serving as a storage site for minerals such as calcium and phosphorus. Understanding the mechanics of bones is essential for preventing and treating bone-related conditions such as osteoporosis, fractures, and arthritis. The study of bone mechanics also provides insight into how bones adapt to changes in loading and other environmental factors, such as aging and disease, and how they repair and regenerate after injury. Besides their apparent biological utility, bones have a hierarchically organized structure [20]. The ligaments and tendons get the principal support from the bones and they can also withstand the fragmentation at certain level. Bones are extremely adaptable to habitual loading at all levels because they can adjust their composition with the mechanical environment and loading regime's components [21]. They store calcium and phosphate and play a vital role in maintaining mineral homoeostasis.

Throughout life, bone tissue goes through continuous substitution and restoration of new tissue. This process is called bone remodeling. Numerous mechanical and biochemical aspects have vital influence on this process. Several cell phenotypes must collaborate for this process to proceed [22]. However, abnormal bone remodeling can be harmful and in fact, most bone diseases are the result of uncontrolled bone remodeling. Basic multicellular units (BMUs), extended formations that move across the surface of bone, are responsible for remodeling. Lack of directional control, a rise in the amount of remodeling cycles, and partial renewal all contribute to abnormal bone remodeling that may cause bone fracture, deformation, acute pain as well as calcium and phosphate homoeostasis [23].

The human skeleton is comprised of two main kinds of bone: cortical bone and trabecular bone (see Figure 2.1). Cortical bone is a dense outer layer of bone, with more porous trabecular on the inside. Almost 80% of the skeleton mass is made of cortical bone [24]. The cortical bone is created from Haversian systems that comprise of concentric lamellae. There are blood vessels in the inner part of the Haversian systems. On the other

hand, trabecular bone (also known as cancellous bone) consists of interconnecting meshwork of trabeculae. The thickness and composition of cortical and trabecular bone vary according to their anatomical location, with long bones generally having a greater thickness of cortical bone compared to vertebrae. Long bones' distal ends, vertebral bodies, and the calcaneus are mostly made of trabecular bone. On the contrary, femoral neck, shaft of the long bones is mostly made of cortical bones [25].

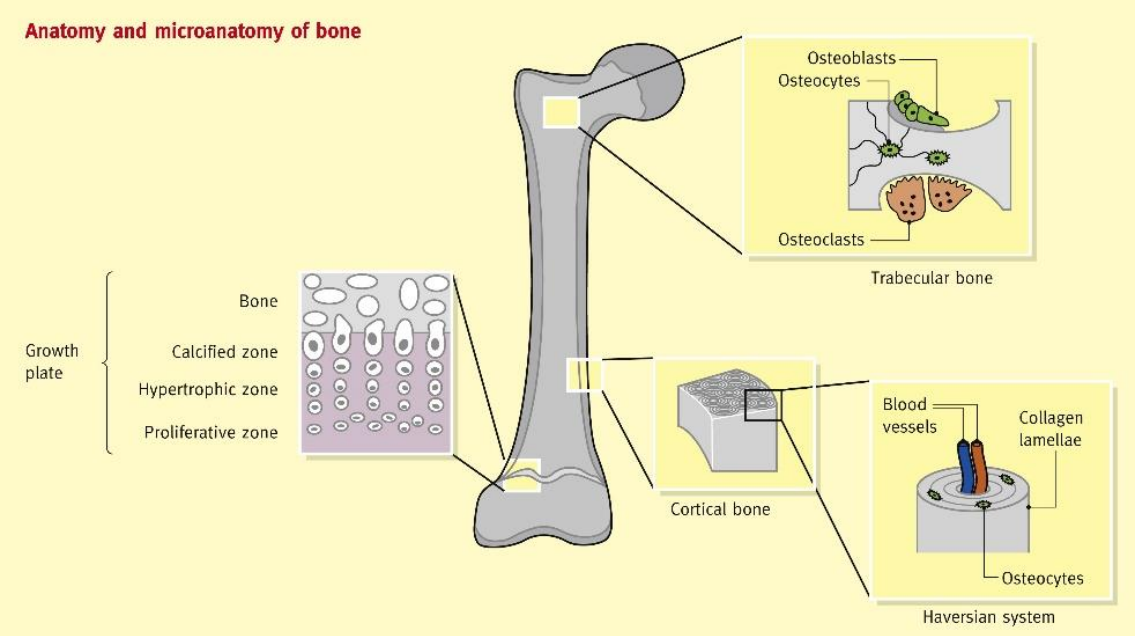

Figure 2. 1. *Anatomy and microanatomy of bone. Here a femur is shown. It has a dense cortical layer with arterial and venous blood vessels through the lamellae, and trabecular bone in center. the trabecular bone is the spongy, porous inner layer of bone tissue that contains a network of interconnected spaces that are filled with bone marrow, which is responsible for producing red and white blood cells as well as platelets. (Copied from Ralston SH. Bone structure and metabolism. Medicine. 2013 Oct 1;41(10):581-5) [25]*

The extracellular matrix (ECM) of bone is comprised of several organic and inorganic components. The inorganic component is mainly crystalline hydroxyapatite: $[Ca_3(PO_4)_2]_3Ca(OH)_2$. The inorganic and organic component covers 60% and 30% of the total tissue by weight respectively. The remaining 10% is mainly water. While the inorganic component of the bone matrix aids in resistance to compression, the organic component aids in resistance to tension [26-28]. It has a dense cortical layer with arterial and venous blood vessels through the lamellae, and trabecular bone in center. the trabecular

bone is the spongy, porous inner layer of bone tissue that contains a network of interconnected spaces that are filled with bone marrow, which is responsible for producing red and white blood cells as well as platelets.

Among the organic components there are 90% Type-I collagen and 10% non-collagenous proteins. Three polypeptide chains make up the triple-helical structure of type I collagen. Every polypeptide chain is made of around a thousand amino acids. Among the polypeptides, there are two similar α1(I) chains and a α2(I) chain. All of these polypeptides have similar structure. However, the α2(I) chain is genetically dissimilar [29].

The mineralization happens when the organic bone components make the structure. This mineralization provides mechanical strength and elasticity to bone. The elasticity mainly originates from bone collagen. Calcium and phosphate, which are deposited in the form of hydroxyapatite [Ca_{10} (PO_4)$_6$ (OH_2)], make up the majority of the bone material. If there occurs deficiency of calcium and phosphate, deformation in mineralization may happen in rickets and osteomalacia. If there are defects in mineralization, this also cause hypophosphatasia that builds up pyrophosphate and hinders the normal mineralization of the bone matrix [28].

We want to make our scaffolds having similar parameter (Young's Modulus, maximum compressive strength, etc.) ranges like trabecular bone or cortical bone. The 3D bioactive scaffolds that are intended to replace bone should have properties similar to those of trabecular or cortical bone, such as porosity, mechanical strength, and biocompatibility. For example, the porosity of the scaffold should allow for the growth of new bone tissue, and its mechanical properties should be similar to those of natural bone to prevent implant failure. In addition, the scaffold should be biocompatible to prevent immune reactions or other adverse effects. By mimicking the properties of trabecular or cortical bone, 3D bioactive scaffolds can provide a suitable environment for the growth and regeneration of new bone tissue. This is important for the development of effective treatments for bone injuries and diseases, as well as for improving the success rates of bone implants.

2.1.2. Natural Bone Healing

Bones can face fatal injuries from trauma, cancer, osteoporosis or other hereditary and diseases at birth (for example, cleft palate) [30]. These diseases make the patient's life hard as they cause discomfort and agony. Sometimes the patients find it difficult to lead

their social life normally. Therefore, it is very important to find the proper treatment to these conditions to help them leading a normal life.

Most of the time the injured place is not healed by the initial healthy tissue. Rather they get healed by the wounded connective tissue. However, bone tissue is exceptional in this case. The bone healing process starts just after the injury. Thus the natural healing closely matches how bones grow in developing animals, but in the case of fracture repair, it also includes the inflammatory stage [30-31].

The natural healing process starts when the inflammatory response is induced. This inflammation is maximum at 48 hours' post-injury and fades away after 7 days. Hematoma development results from the soft tissues and the periosteum being spoiled. Additional hemorrhage is restricted by this hematoma. The hematoma gives a way for cellular migration by acting as a fibrin [32,33]. Macrophages are attracted by the inflammation to the injured area and this starts the healing procedure. A reparative callus tissue made of fibrous connective tissue, blood vessels, cartilage, woven bone, and osteoid grows at the fracture site once the tissue debris is removed. In the injured area the increased proliferation of mesenchymal cells and fibroblasts happens due to the delivery of growth factors and cytokines as a consequence of the alteration in the nearby area such as temperature, oxygen saturation, pH etc. Osteoprogenitor cells are transformed from some mesenchymal cells. Chondrogenesis causes the formation of a soft callus. The ECM then begins to calcify. Woven bone is then formed by the angiogenesis process that converts into perfectly grown bone and bone marrow. Following that, normal bone remodelling occurs [31,32].

Intramembranous ossification and intracartilaginous bone formation are two pathways which from the bone. Often these injuries recover via the intracartilaginous channel, although bone damage in the skull and clavicles recover via the intramembranous channel [31]. According to some studies, intramembranous bone can be formed in the body areas where bone cannot form conventionally and this bone formation is influenced by bone morphogenic protein-2 (BMP-2). Although bone repairs faster unlike various tissues, the natural bone restoration mechanism has limitations since it cannot mend inherited flaws, critical sized defects, or disease-related abnormalities. Novel therapies are essential for enhancing the living quality of patients suffering from these disorders [31].

The 3D scaffolds that we are printing must have the natural healing properties that can promote tissue repair and regeneration. Natural healing properties can provide a more

effective and sustainable solution for tissue repair and regeneration, improving the quality of life for patients with various injuries and diseases. The scaffolds are designed to support the growth and regeneration of new tissue in the body, which is important for the treatment of various injuries and diseases.

2.1.3. Wolf's Law for Bone Remodeling

In the 19th century, German surgeon and anatomist Julius Wolff stated Wolff's law which explains the response of the bone when stress is applied to it. According to Wolff's law, bones go through significant changes when they try to resist the applied strain. Basically, the internal structure of bones gets firm so that they can withstand external pressure. Wolff's law also describes the opposite case. In the opposite case, when the applied weight on the bone gets reduced, the bone gets fragile and lighter. If the weight of the bone significantly decreases, the bone might need to be replaced at some point.

An ideal 3D bioactive scaffold for bone tissue engineering should have a balance between compliance and stiffness. This can be achieved through careful selection of materials, fabrication techniques, and scaffold design. For example, the use of porous materials with controlled pore size and distribution can provide a balance between strength and porosity, which is necessary for supporting the growth of new bone tissue. In addition, the use of materials with high fracture toughness and fatigue resistance can improve the long-term durability of the scaffold. Overall, we need to design our scaffolds with appropriate mechanical properties is essential for promoting bone growth and preventing failure or complications. By considering factors such as compliance, strength, and durability, researchers can develop scaffolds that provide optimal support for the growth and regeneration of new bone tissue.

Wolff's law is not appropriate for every situation. It has been discovered that instead of explaining a specific experience, it depicts a variety of processes taking place inside the bones. Initially Wolff's law depicts only specific cases that makes the bones firmer. When the bone structure changes that has direct impact on bone mass, the bones get firmer.

There are several advantages of weight resistance exercises, such as, increase in bone density.

In Figure 2.2. (A), the bone modeling by drift in shown. Here, the primary form of a newborn baby is defined by the solid line. To maintain its structure as it expands in both width and length, modeling drifts shift its edges in tissue area, as seen by the dotted line. Development drifts generate and direct new osteoblasts to construct certain areas. New osteoclasts are produced by resorption drift so that bone can be eliminated from other surfaces. A modified drift strategy can repair a baby's fracture malunion. A baby's fracture malunion can be repaired by the drift pattern that is shown in Figure 2.2. (B). On the right the crossectional view is presented where the endocortical and periosteal drifts that perform the repair are seen. Figure 2.2. (C) shows how the drifts in (B) may shift the entire section to the right of the reader. The bone's bending area is decreased in this way but does not completely disappeared. Drifts consist of capillaries, precursor and supporting cells, as well as some drifting cells. Drifts are generated if they are required. These are multicellular organisms; whose primary function is to reduce the maximum bone strains [33-34].

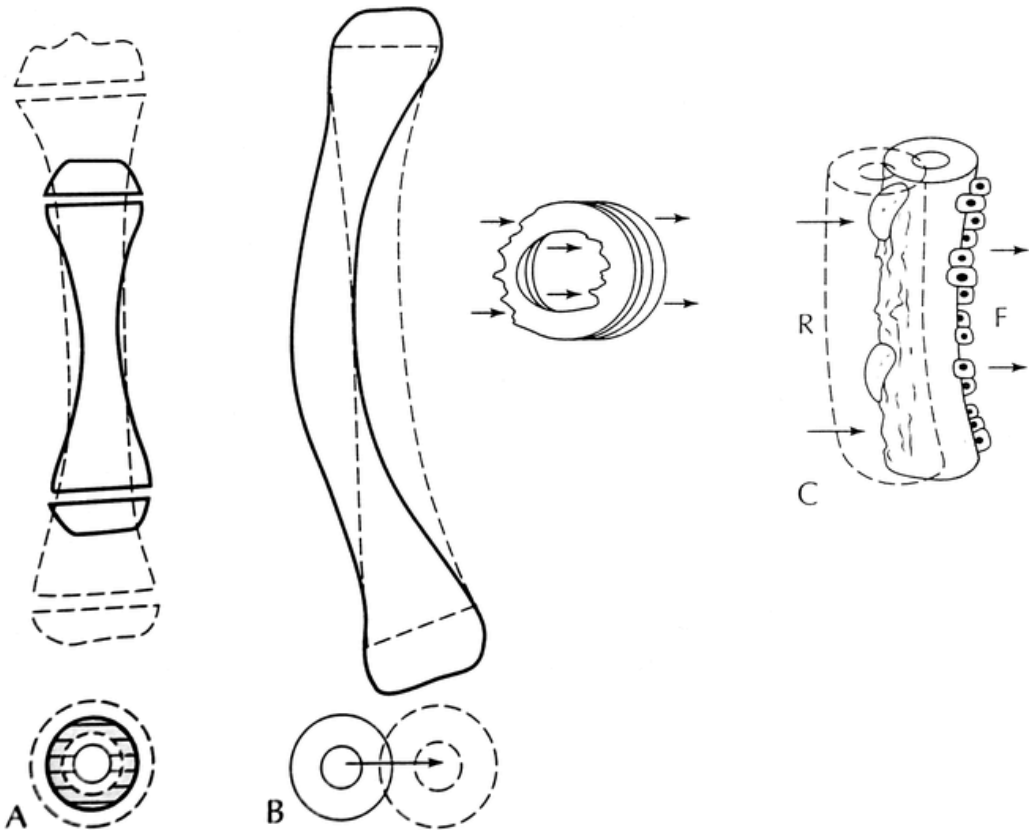

Figure 2. 2. *Bone modeling drift shown in a newborn baby's bone (Frost HM. A 2003 update of bone physiology and Wolff's Law for clinicians. The Angle Orthodontist. 2004 Feb;74(1):3-15) [33]*

Bone mass loss is more common in women than men. For instance, a man can lose 18% of his bone mass at the age of eighty while a woman can lose up to 50% of her bone mass at the same age. This is main reason for which osteoporosis is more common in women. When a person has osteoporosis, his bones get deteriorated acutely and bones become fragile gradually. Wolf's law can be used for the treatment of osteoporosis. Light and moderate exercises are proven advantageous for the treatment of osteoporosis.

Wolff's law is also applied for the treatment of bone fractures. Many physical therapies used to heal fractures follow Wolff's Law, arguing that controlling the load on the bone results in the best restoring and strengthening. Nevertheless, physical exercises that are supervised by expert physiotherapists are recommended [35].

2.2. Mechanical Properties of bone

The mechanical properties of a material can be described by the stress-strain curve that is determined by applying uniaxial force until it is broken. The stress-strain curve provides a quantitative measure of a material's mechanical properties, including its strength, ductility, toughness, and resilience [36-37].

Here is the stress-strain curve of generic bone tissue (see Figure 2.3). The x axis of the curve represents the strain and y-axis represents corresponding stress of bone tissue. In the elastic region of the curve, the bone returns to its original state if the applied load is eliminated. After the elastic region, the applied load causes a permanent change in the bone (from B to C in Figure 2.3). This is denoted as plastic deformation. The ultimate

elongation defines the maximum force that bone can withstand before rupture. The properties of the bone and skeletal structure and the direction of the applied force dictate the maximum load sustainable by the tissue.

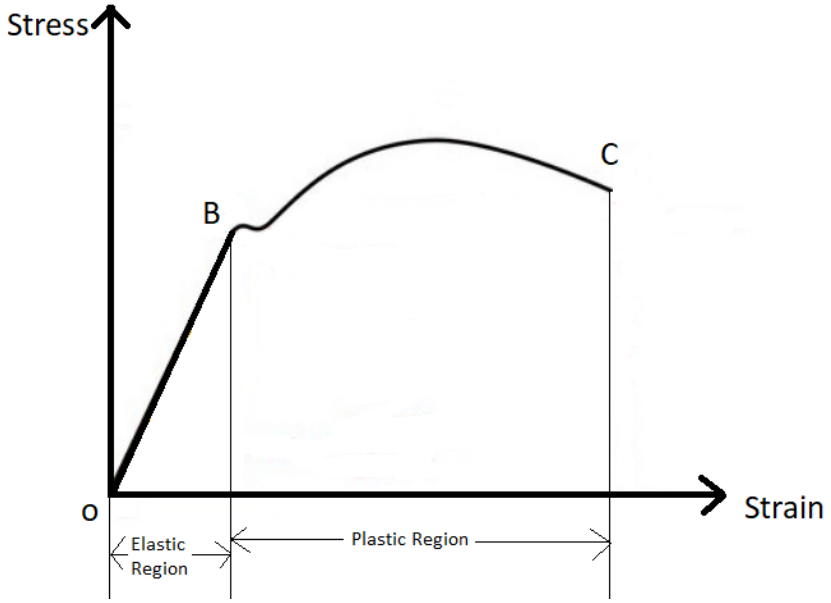

Figure 2. 3. *A typical stress-strain curve of bone tissue*

The slope of the linear part of the curve (OB in Figure 2.3) is the Young's Modulus. Young's modulus, also known as the modulus of elasticity, is a material property that describes the stiffness of a solid material. It is defined as the ratio of stress (force per unit area) to strain (change in length per unit length) in the linear region of deformation, under the assumption of isotropic, homogeneous, and elastic behavior.

The maximum compressive stress of a material is the largest compressive stress that the material can withstand before it fails or is permanently deformed. In Figure 2.3 the compressive stress at point B is the maximum compressive strength. The strain at point B is the compressive strain at maximum compressive strength. To describe the mechanical properties of a material, these parameters play vital roles.

2.3. Bioactive Glasses

Hench developed 45S5 bioactive glass in 1969. Bioactive glass has the ability to promote the growth and regeneration of new bone tissue. Moreover, its versatility in terms of fabrication and design, make it a promising material for the development of effective treatments for bone injuries and diseases. Hence, bioactive glass was developed because it is an important material for bone replacement because of its bioactivity, biocompatibility, and mechanical properties. The first bioactive glass was made in order to produce implants that could endure the body's adverse conditions and still build a solid link or contact with the target tissues. The first clinical application of bioactive glass (45S5) was to help deaf individuals hear again. Monolithic implants composed of 45S5 were used to substitute the middle part of ear bones that were injured [38]. Since then, scientists have continued to develop bioactive glass scaffold materials for bone restoration [39–40].

Bioactive glass can induce bone cell growth and make the attachment to hard and soft tissues [41,42]. The capacity of a substance to generate a HA-like surface layer in vitro when submerged in a simulated body fluid (SBF) is frequently used to predict its bioactivity [43].

When bioactive glasses are implanted, they perform particular processes that cause the development of an amorphous calcium phosphate (ACP) or crystalline hydroxyapatite (HA) phase on the glass's interface. This ACP and HA phase plays the main role in creating powerful bond with the neighboring tissue [39]. It has also been found that bioactive glasses emit ions which not only trigger the activation of osteogenic genes but also induce angiogenesis [44-48]. The bioactive glasses can easily control the chemical configuration through ion exchange. This process involves the exchange of ions between the bioactive glass and the surrounding environment, which can result in changes to the chemical composition and properties of the material. As a result, their rate of degradation makes them desirable in making the 3D scaffolds. Glass scaffolds with varied rate of degradation can be designed to mimic bone regeneration and remodeling. However, the main drawback of bioactive glasses are their poor mechanical properties which is critically important in repairing bone injuries [40]. Recently published studies have demon-

strated that by adjusting the formulation, manufacturing, and sintering conditions, bioactive glass scaffolds can be produced with preconfigured pore topologies and durability similar to human trabecular and cortical bones [49-51].

Bioactive glass scaffolds are widely used in tissue engineering and regenerative medicine for the repair or replacement of damaged or diseased tissues. They offer several advantages over traditional scaffold materials, such as metals or polymers, including their biocompatibility, ability to stimulate tissue regeneration, and ability to integrate with the surrounding tissue.

Bioactive glass scaffolds are commonly used in bone tissue engineering to promote the regeneration of bone tissue. The scaffolds provide a porous structure that allows for the infiltration of cells and nutrients, promoting the growth of new bone tissue.

Bioactive glass scaffolds can also be used in the regeneration of cartilage tissue. The scaffolds can be designed to mimic the mechanical properties of cartilage, promoting the growth of new tissue and reducing the risk of rejection. Bioactive glass scaffolds can be used in the regeneration of blood vessels. The scaffolds can be designed to promote the growth of endothelial cells, which form the lining of blood vessels, and smooth muscle cells, which provide structural support.

Bioactive glass scaffolds can be used in the development of dental implants. The scaffolds can be used to support the growth of new bone tissue, promoting the integration of the implant with the surrounding bone. Bioactive glass scaffolds can be used in the treatment of chronic wounds, such as diabetic ulcers. The scaffolds can be designed to promote the growth of new tissue, reducing healing time and improving the overall outcome.

Overall, bioactive glass scaffolds offer a versatile and effective solution for a wide range of tissue engineering and regenerative medicine applications. Their ability to promote tissue regeneration and integration with the surrounding tissue makes them a valuable tool for improving patient outcomes and quality of life [52-55].

Among bioactive glasses, borosilicate glasses have shown great potential as materials for biomedical applications, as they exhibit faster and more complete conversion kinetics into hydroxyapatite compared to traditional silicate glasses. Using boron-containing glasses based on the 45S5 formulation implanted in rat tibia bone marrow found that these glasses promoted bone formation more effectively than the pure silicate 45S5 [8,56].

3. MATERIALS AND METHODS

This chapter describes the materials and methods we used to fabricate a bioactive glass scaffold. It describes the process of making the bioactive glass, making the ink for 3D printing, sintering and stacking the scaffolds with metallic screws and titanium plates, and test their mechanical properties.

3.1. Preparing The Bioactive Glass

In Tampere University Jonathan Massera and his group is working with the B12.5 MgSr bioactive glass that has several useful properties such as: high porosity, not crystalizing after sintering process [57]. However, the ordinary 3D scaffolds made from this glass are not stackable. So, we developed a new approach in which we used the same B12.5 MgSr bioactive glass to print the scaffolds but they will be stackable. The bioactive glass had two components, an inorganic glass component, and an organic component (pluronic gel). The pluronic gel held the glass particle together to so that a 3D printable ink could be prepared. The scaffolds were allowed to dry after printing. Then they were sintered and after the sintering the organic component was burnt off, thus remaining only the bioactive glass in the scaffolds.

The expected mol% formation of the bioactive magnesium strontium glass (B12.5 MgSr) is 47,12 SiO_2 – 6,73 B_2O_3 – 6,77 CaO – 22,66 Na_2O – 1,72 P_2O_5 – 5 MgO – 10 SrO. The

required materials that were used for the preparation of 100 g B12.5 MgSr are stated in Table 3.1.

Table 3.1. *Ingredients used in preparation of 100 g B12.5 MgSr*

Ingredients	Mass (g)
SiO_2	43.121
Na_2CO_3	36.582
$SrCO_3$	22.497
H_3BO_3	12.685
$CaCO_3$	10.327
$(NH_4)H_2PO_4$	6.037
MgO	3.076

These materials are weighted carefully with Mettler Toledo PM400 scale. Then they are mixed in a ceramic mortar. The mixture was transferred into a platinum crucible. The temperature profile used for the melting is shown in Table 3.

Table 2.2. *Temperatures of glass melting Temperature*

Temperature (°C)	Time (min)
250	15
650	30
850	30
1250	30

The molten glass was casted into a graphite mold. The glass was then transfer to the annealing furnace to release the residual stress. The annealing temperature was at 450 °C, r and annealing time 6 hours.

For 3D printing, B12.5 MgSr glass was crushed into particles with size smaller than 38 m. The glass was milled with FRITSCH milling machine and then sieved with a Gilson USA standard test sieve.

3.2. Preparing the Ink for 3D Printing

The Pluronic is required to make the bioactive glass because it works as the binder. 25% Pluronic and the glass is mixed so that a 3D printable ink can be prepared. The Pluronic is eliminated after the sintering process because the Pluronic will be burnt off in the sintering oven. To prepare the 25% Pluronic we needed Pluronic F-127 (Sigma-Alrdich) and distilled water. In a plastic container 12.5 g of Pluronic and 37.5 g of distilled water were added. Then a magnetic stirrer was kept in the container. Then we sealed the container and added the container in the ice bath. The ice was replaced every several hours, and the solution was kept in the ice bath overnight until transparent. Once the Pluronic was prepared, it was always refrigerated at a temperature 4°C because Pluronic gets solidified if the temperature is not maintained properly. This was because Pluronic F-127 25% has a glass transition temperature of 15-20°C [58].

First, we have to calibrate the weight scale. Then with the scale we take around 3.36 g MgSr to a plastic bottle and add 2.8 to 3 g Pluronic to the bottle with a plastic piped. At this time, we must take this measurement as precisely as possible. We also must make sure that there are no bubbles. To mix Pluronic and glass powder we use Vibrofix VFI mixer (see Figure 3.1). To have a proper mix, we should keep the rpm value as 2500 rpm on the Vibrofix and touch the bottle to it for 30 seconds and then keep the bottle in the ice bath. We have to repeat this step 8-10 times until the ink was homogeneous and bubble free. As Pluronic gets solidified if it is not cooled, the bottle is kept in the ice bath during intervals so that the mixer does not get solidified. Then the ink is transferred to the syringe and inserted to 3D printing cartridge. The cartridge was then covered with parafilm. The prepared ink was kept in the room temperature for around 1 hour so that perfect viscosity was obtained.

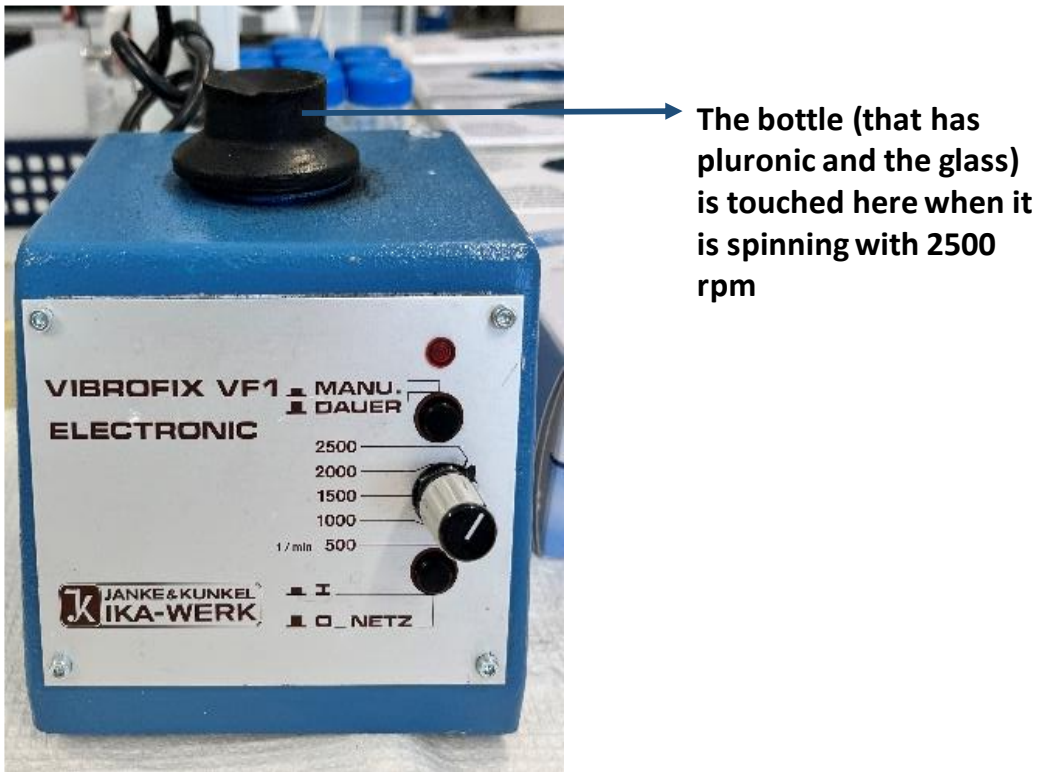

Figure 3. 1. *Photograph of the Vibrofix VFI mixer. The bottle (that has pluronic and the glass) is touched on the black part on the top when it is spinning with 2500 rpm*

3.3. 3D Printing

The cartridge was connected to the nScrypt 3Dn – TABLETOP printer (see Figure 3.2(A)). Then the parafilm was detached from the cartridge and the tip with 0.41 mm of nozzle size was added to the cartridge. A plastic film was used as support for the printer

(see Figure 3.2(B)). the material feed range was from 18 psi to 25 psi depending on the temperature and humidity in the room.

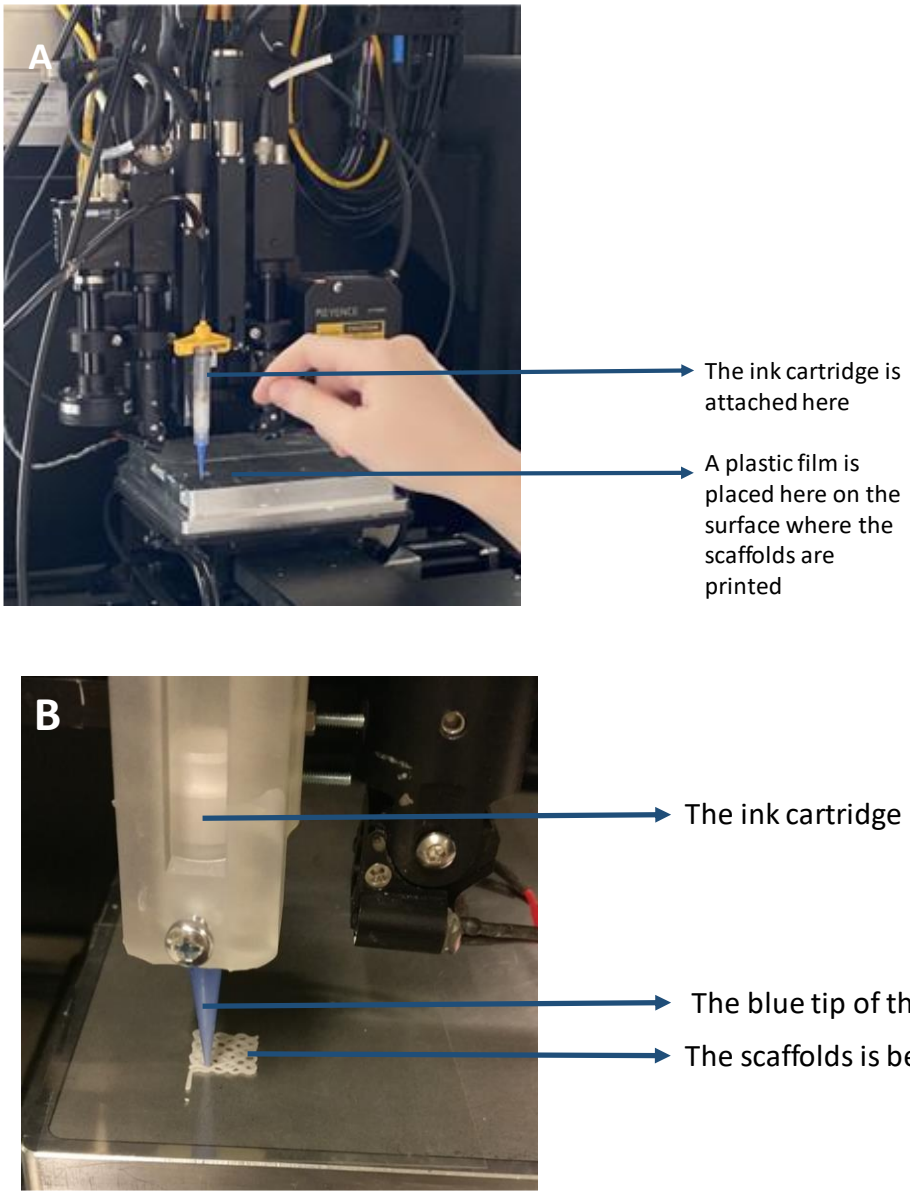

Figure 3. 2. (A) *The nScrypt 3Dn-TABLETOP 3D printer that was used to robocast the scaffolds* ***(B)*** *The scaffold is being printed by the ink cartridge with 3D printer*

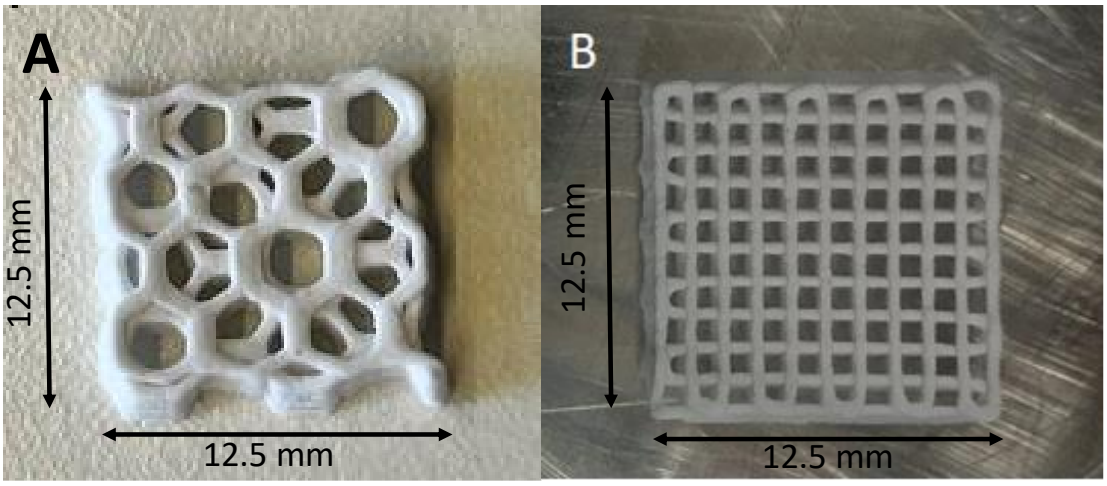

Figure 3. 3. *Photograph of Printed (not sintered) Hexagon (A) and logpile (B) 3D Scaffold (Around 12.5 mmx12.5 mmx 2.3 mm)*

We printed several hexagon scaffolds and chose those scaffolds that have similar weights (see Figure 3.3 A). We also printed logpile scaffolds (see Figure 3.3 B) with similar length, width and height of the hexagon scaffold to measure the mechanical strength and compare to that of the hexagon scaffolds. The scaffolds were stored at room temperature at least for 24 hours after printing to be dried completely.

We also stacked two hexagon scaffolds with a titanium plate on top and one in the bottom (see Figure 3.4) so that they get better mechanical strength. The scaffolds were stacked with stainless steel screws. The diameter of the screws was 1.5 mm. The plates had several holes to mimic the mesh look.

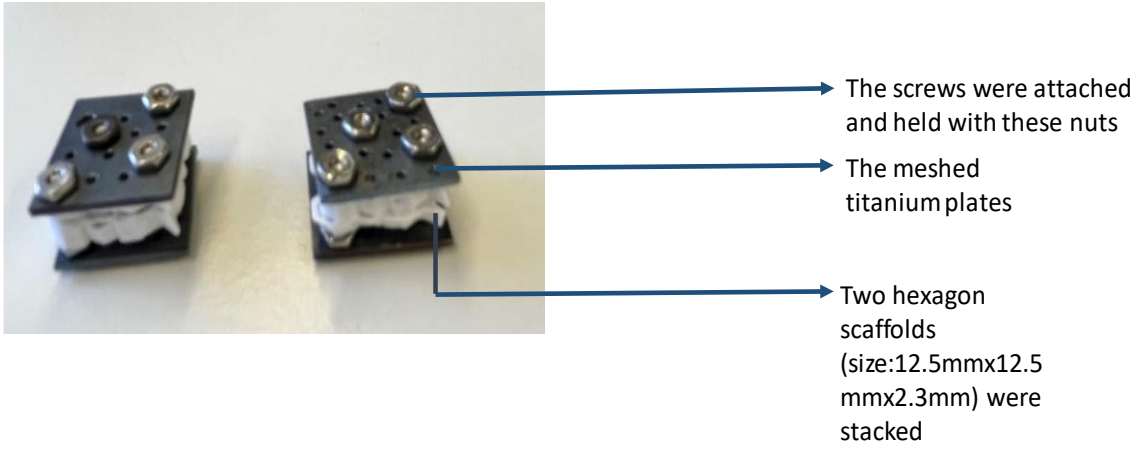

Figure 3. 4. *Photograph of the stacked hexagon scaffolds. The hexagon scaffolds were printed and sintered and then they were stacked with the help of stainless steel screws with a titanium plate on the bottom and on the top. The scaffolds size was Around 12.5 mmx12.5 mmx 2.3 mm and the plate size was around 15 mmx 15 mm.*

3.4. Sintering the Scaffolds

After the scaffolds were dried, we needed to sinter them. This was important because the sintering process eliminated the Pluronic. For B12.5 MgSr the sintering temperature is 542°C [57]. For sintering we used Nabertherm oven (see Figure 3.5). The heating rate was 1°C/min as the heat rate until the oven reach 309°C. The heating rate was then set to 5°C/min until the oven reach 542°C. The temperature was kept for 1 hour. Finally, the temperature was decreased using the furnace inertia. The scaffolds were removed once the temperature was closed to room temperature (22°C).

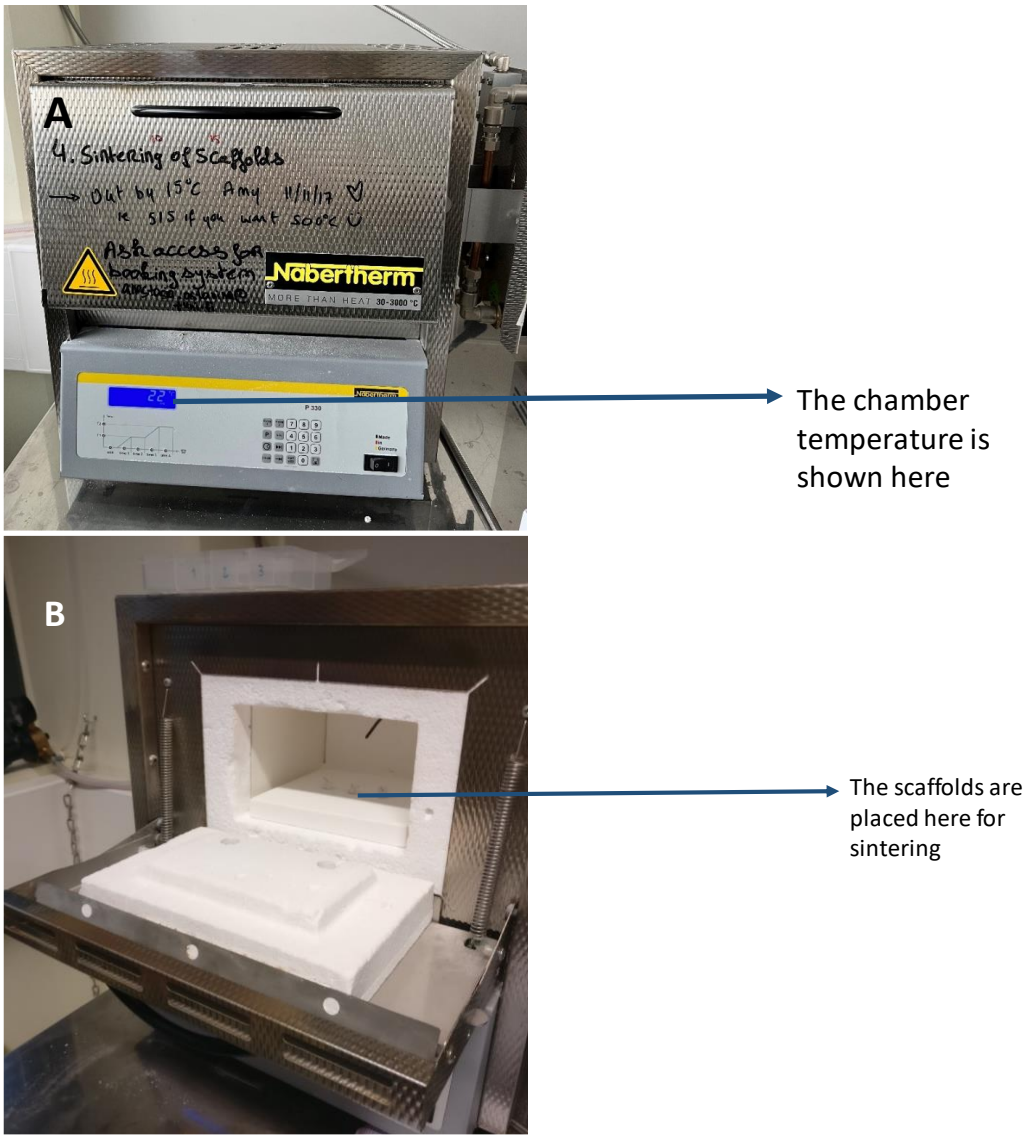

Figure 3. 5. *Photograph of (A) outside and (B) inside of the Nabertherm Sintering Oven*

3.5. Mechanical Testing

Pluronic was burnt off from the scaffolds through the sintering process. The scaffolds were removed from the oven when the chamber temperature reached the room temperature. Then, the mechanical testing of the sintered scaffolds was done. For the mechanical testing we used five to six samples of each type (Single hexagon samples, single logpile samples, stacked hexagon samples). The mechanical testing was done after the scaffolds were sintered and rested for at least one day. Then we measured the heights, widths and thickness of the samples. We used Instron Electropuls E1000 with 2kN cell for the mechanical testing (see Figure 3.6). For the measurement, Bluehill universal software was used. We kept the sample on the plate of the machine where they were compressed. The displacement rate was 0.5 mm/min. Before starting the compression, the force of the machine was balanced and displacement of the machine was zeroed. We used this software to measure compressive strength at yield, compressive strain at yield, maximum compressive strength, Young's modulus, and compressive strain at maximum compressive stress.

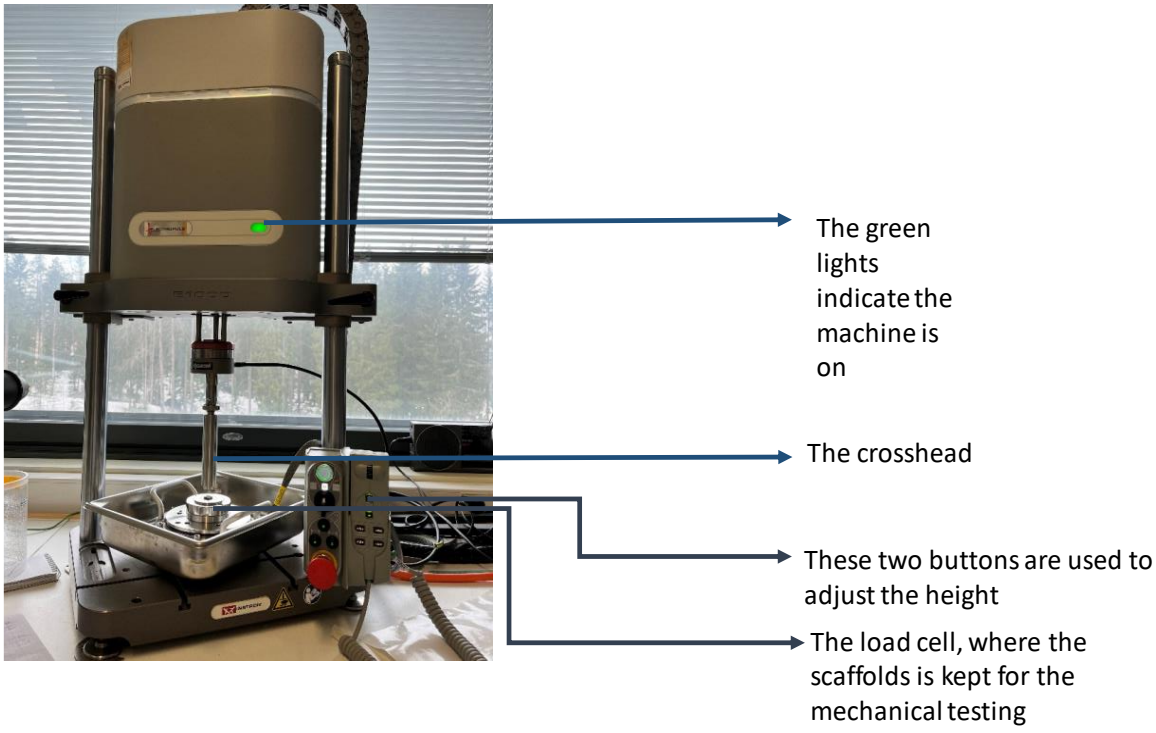

Figure 3. 6. *Photograph of the Instron Electropuls E1000 that was used for mechanical testing of the scaffolds.*

4. RESULTS AND DISCUSSION

The detailed process of making the scaffolds and mechanical testing are described in the previous section. In this chapter, the results were analyzed and discussed. The weight difference in the sintering process, the porosity of the scaffolds, stress-strain curve of the scaffolds and the comparison of the scaffolds are described in this chapter.

4.1. Weight loss of the scaffolds after sintering

We tried to print the scaffolds with similar weights. For hexagon and logpile both scaffolds, we kept all the variables same so that we get scaffolds of similar weight. Their weights before and after sintering are stated in table 4.1 and table 4.2. We can see there is a decrease in mass after sintering for both the types of scaffolds. This was expected because sintering process removes the Pluronic from the scaffolds. In fact, after sintering the mean weight loss for the hexagon scaffold is 44.8 mg and the standard deviation is 3.3 mg.

Table 4.1. *Weight of the hexagon scaffolds before and after sintering*

Weight of the hexagon scaffolds before sintering (mg)	Weight of the hexagon scaffolds after sintering (mg)
223.63	182.0
211.90	172.7
260.54	211.8
251.85	205.20
253.31	206.23
249.63	203.27

Similarly, for the logpile scaffolds after sintering the mean weight loss is 60.2 mg and the standard deviation is 5 mg.

Table 4.2. *Weight of the logpile scaffolds before and after sintering*

Weight of the logpile scaffolds before sintering (mg)	Weight of the logpile scaffolds after sintering (mg)
363.2	294.35
329.06	266.84
298.35	243.46
321.49	262.05
301.41	245.61

4.2. Determining the porosity of the scaffolds

Porosity is the percentage of the void area in a scaffold. The porosity of the bioactive glass scaffolds is an important parameter when we consider in vivo and in vitro bone regeneration. In bioactive scaffolds, porosity is critical because it affects several important factors, such as nutrient and oxygen transport, waste removal, cell attachment, and proliferation. The porosity of a scaffold also determines the rate of degradation and resorption of the scaffold material, which is crucial for allowing new tissue to replace the scaffold. Furthermore, the porosity of the scaffold affects the mechanical properties of the scaffold, such as its compressive strength and elasticity. An ideal bioactive scaffold should have a porosity that is high enough to allow cells to grow and differentiate but low enough to provide sufficient mechanical stability and support for the growing tissue [59]. The porosity of produced scaffolds is typically from 70 to 90% [60-61].

There are several processes to calculate the porosity of the scaffolds. According to gravimetry, the porosity is determined by equation,

$$P = \frac{\rho_{Scaffold}}{\rho_{Material}} \times 100\% \quad \text{.....(1)}$$

Here P is the porosity of the scaffold, $\rho_{Material}$ is the density of the scaffold material and $\rho_{Scaffold}$ is the average density of the scaffold including the void volume.

We took five samples of the hexagon and logpile scaffolds. We measured the length, width and height accurately with Vernier caliper to determine the volume. By multiplying the length, width and height we know the volume of the scaffolds. Then we weighted the samples. Then the density of each scaffold ($\rho_{Scaffold}$) can be determined by diving the weight of each sample with the corresponding volume. On the other hand, we know the density of B12.5 MgSr glass, which is 2.64g/cm^3 ($\rho_{Material}$). Then the porosity can be calculated with the help of Equation 1.

The mean porosity of the logpile samples is 72.4% and the standard deviation is 4.2%. By contrast, the mean porosity of the hexagon samples is 78.9% and the standard deviation is 2%.

We also tested some ordinary logpile samples that are generally used by Jonathan Massera's group. We took some of the ordinary logpile scaffolds from Agata Szczodra and tested their mechanical properties. Agata already measure the porosity of those ordinary logpile scaffolds by micro-computed tomography (µCT). According to her data,

the mean porosity of the ordinary scaffolds was 43% and the standard deviation was 2.7%.

4.3. Stress-strain curve of the single hexagon scaffolds

We performed the mechanical testing of the single hexagon scaffolds (see Figure 3.3 A) to understand their mechanical properties properly. Here, Figure 4.1 is a representative stress-strain curve of the single hexagon scaffolds. This Figure is the graphical representation of the behavior of the hexagon scaffolds under a compressive load. The curve plots the amount of stress in MPa on the y-axis and the corresponding amount of strain in percentage on the x-axis. Originally the instrument measures in terms of force (N) Vs displacement (mm) and then the values are converted into stress versus strain. We plot the applied force in N on the right side of the y axis. The displacements values in mm are also shown in the curve along with the displacement (%) values (see Figure 4.1). In Figure 4.1, we see initially the compressive stress was increasing linearly until the compressive strain reached to 1.5 % (peak (i) in Figure 4.1). At this point (i) the force was 4.6 N and the displacement was 0.1 mm. From 0 to this point (i), the stress was proportional to strain. This is the elastic region of the scaffold that means in this region the scaffold faced no deformation. As the load keeps increasing, there was a sudden decrease in compressive stress after the peak (i). This dramatic drop in compressive stress means the scaffold faced a fracture. The compressive stress reached the maximum point that represents the ultimate tensile strength (0.04 MPa) of the scaffold that was achieved just before the fracture. After the first fracture, the stress kept decreasing and again started increasing. Thus the scaffold faced some periodic collapses and was broken several time. Every sudden decrease of the compressive stress means that the scaffold is facing a fracture. At the points labeled (ii), (iii), (iv) and (v), there were sudden decrease in the compressive stress that refers the fractures that the scaffolds faced during the experiment. When the experiment was done, there were several cracks in the scaffold (see Figure 4.2).

Here, the single hexagon scaffold faced its first fracture at point (i) where the maximum compressive strength was 0.04 MPa and the compressive strain was 1.51%. We see the scaffold face periodic collapses at point (ii), (iii), (iii), (iv), (v) and finally when the compressive strain was 20%. At this point the compressive stress was 0.11 MPa and the force was 13 N. This is the maximum compressive strength that the scaffold achieved before getting completely broken. The mechanical test was ended when the compressive strain was 20%. If we see Figure 4.3, only sample C was stopped at the compressive

strain 10% because the machine decided to stop the testing as the scaffolds were broken severely and achieved maximum compressive strength already.

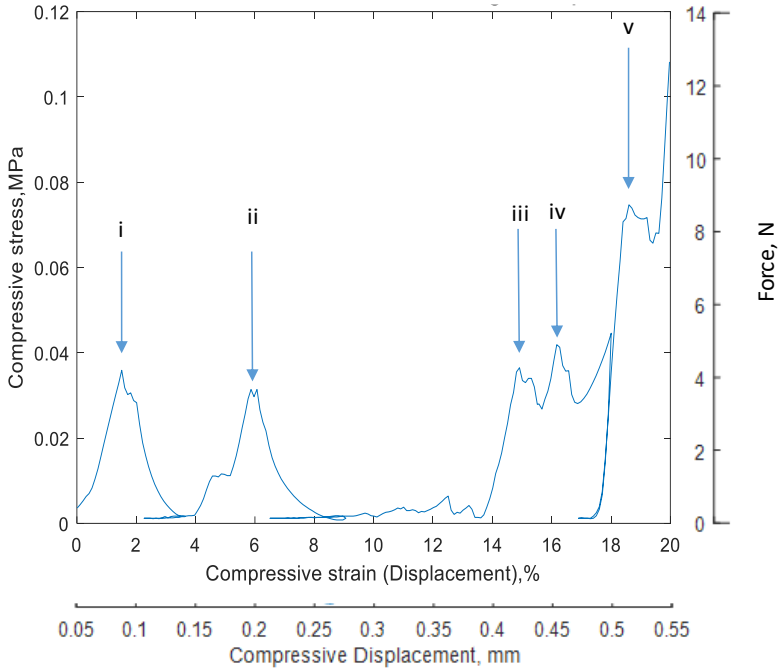

Figure 4 1. *Stress vs strain curve (and load displacement on second axes) for a representative hexagon sample. The points labeled with Roman numerals represents the multiple collapses of the scaffold representative*

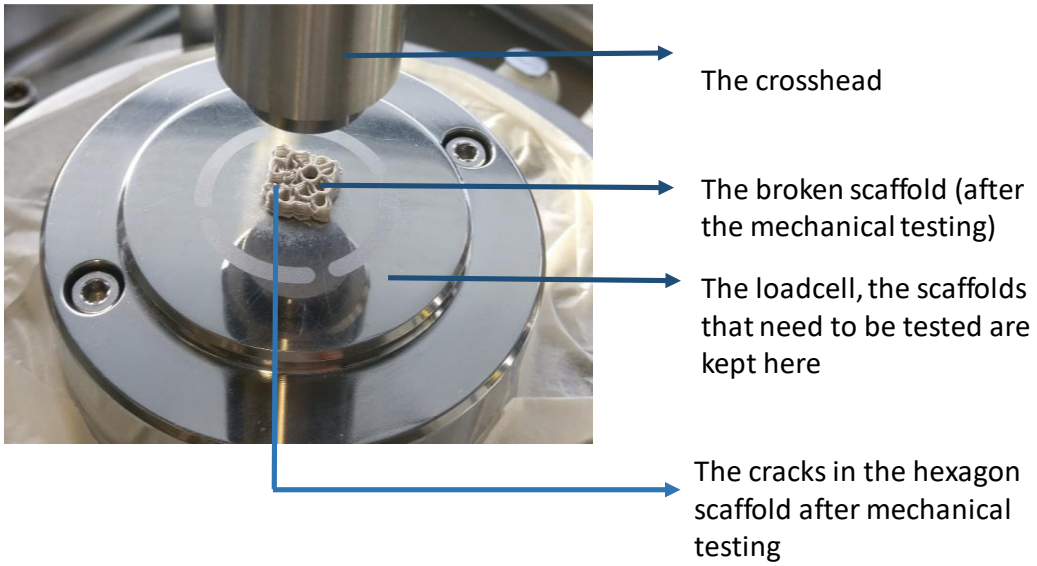

Figure 4 2. *Photograph of the broken hexagon scaffold after the experiment*

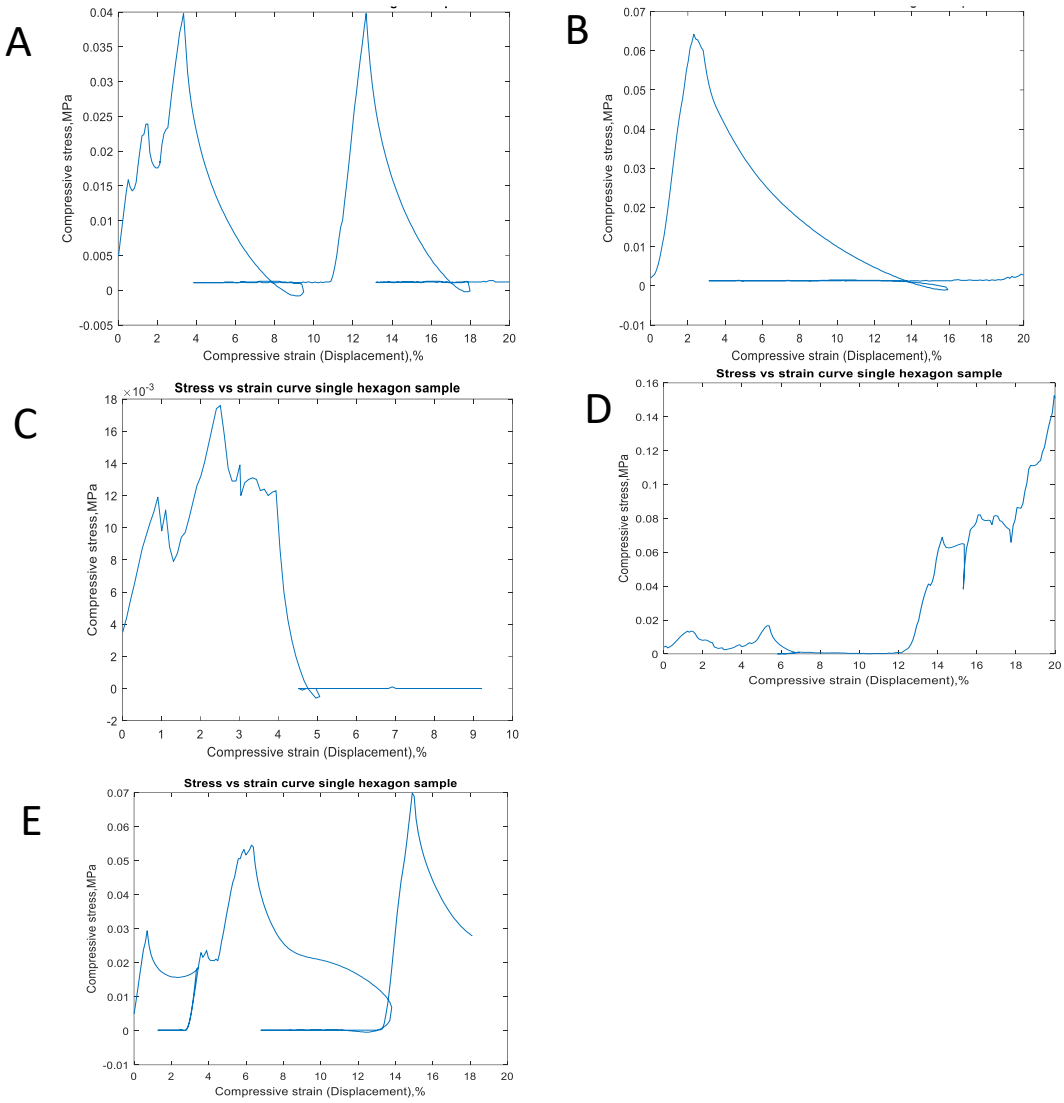

Figure 4 3. *The stress-strain curves of single hexagon sample 2,3,4,5,6 that are shown as A, B, C, D, E respectively*

We tested five more hexagon samples in the similar way. The stress versus strain curves of these scaffolds are shown in Figure 4.3. The sudden drop of the compressive stress indicates the fracture that happened during the experiments. Several periodic peaks mean, there are several cracks in the scaffolds. We calculated the Young's modulus, the first maximum compressive stress, the maximum compressive strength achieved by the sample before complete failure and the compressive strain at the maximum compressive stress for each graph (Figure 4.3 A to E). The Young's modulus is basically the slope of the first linear part of the figure. The values for the single hexagon scaffolds are represented in Table 4.3.

Table 4.3. *Young's Modulus, maximum compressive strength and maximum compressive strain of the single hexagon samples*

	Young's Modulus (MPa)	First Maximum Compressive Strength (MPa)	Maximum Compressive Strength before ultimate failure (MPa)	Maximum Compressive Strain (%)
Sample 1	2.9	0.04	0.11	1.51
Sample 2	2.3	0.02	0.04	0.05
Sample 3	3.6	0.06	0.06	2.32
Sample 4	0.9	0.01	0.02	0.91
Sample 5	1.2	1.21	0.15	0.01
Sample 6	3.4	0.03	0.07	0.70

4.4. Stress strain curve of the single logpile samples

We printed five logpile scaffolds around same length, width and height as the hexagon scaffolds (see Figure 3.3 B). We did the mechanical testing similarly as we did it for the hexagon scaffolds. Here, Figure 4.4 represents the stress-strain curve of the single logpile scaffolds. The curve plots the amount of stress in MPa on the y-axis and the corresponding amount of strain in percentage on the x-axis and this curve represents the behavior of the logpile scaffolds when compressive load is applied on them. The applied force (N) is shown on the right side of the curve on y axis. The displacement values in mm are also shown (see Figure 4.4).

In Figure 4.4, the compressive stress was increasing linearly until the compressive stress was 0.01 MPa and the compressive strain reaches 1.8 % (peak (i) in Figure 4.4). At this point (i) the force was 1.9 N and the displacement was 0.6 mm. From 0 to this point (i), the stress was proportional to strain and so this is the elastic region of the scaffold. During this time, there were no fracture in the scaffolds. The scaffolds actually achieved its first maximum compressive strength at point (i). Then after the point (i) in Figure 4.4, the compressive stress suddenly decreased dramatically that refers to the first fracture in the scaffold. Then the compressive stress again started to increase till point (ii) (see Figure 4.4) and dropped again suddenly. At point (ii) the scaffolds achieved its second maximum compressive strength. Here, the test the compressive strain was 0.01 and the compressive strain was 7%. The force at this point (peak (ii) in Figure 4.4) was 1.7 N and the displacement was 0.7 mm. After point (ii), the scaffold faced some minor cracks.

Unlike the hexagon scaffolds, the logpile scaffolds did not face too many fractures and there were some cracks that have been shown in figure 4.5.

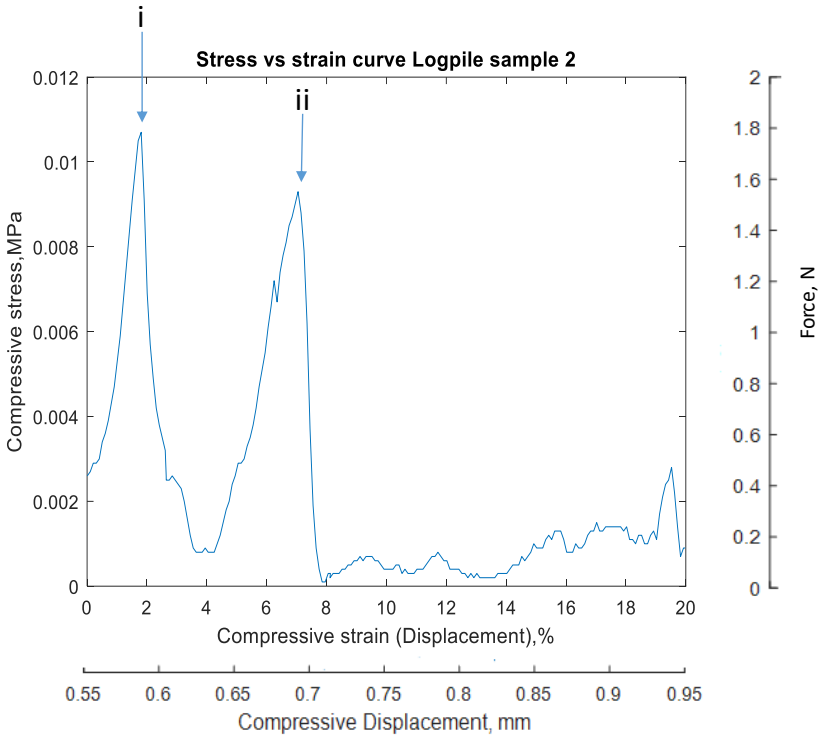

Figure 4 4. *Stress vs strain curve (and load displacement on second axes) for a representative logpile sample. The points labeled with Roman numerals represents the multiple collapses of the scaffold representative*

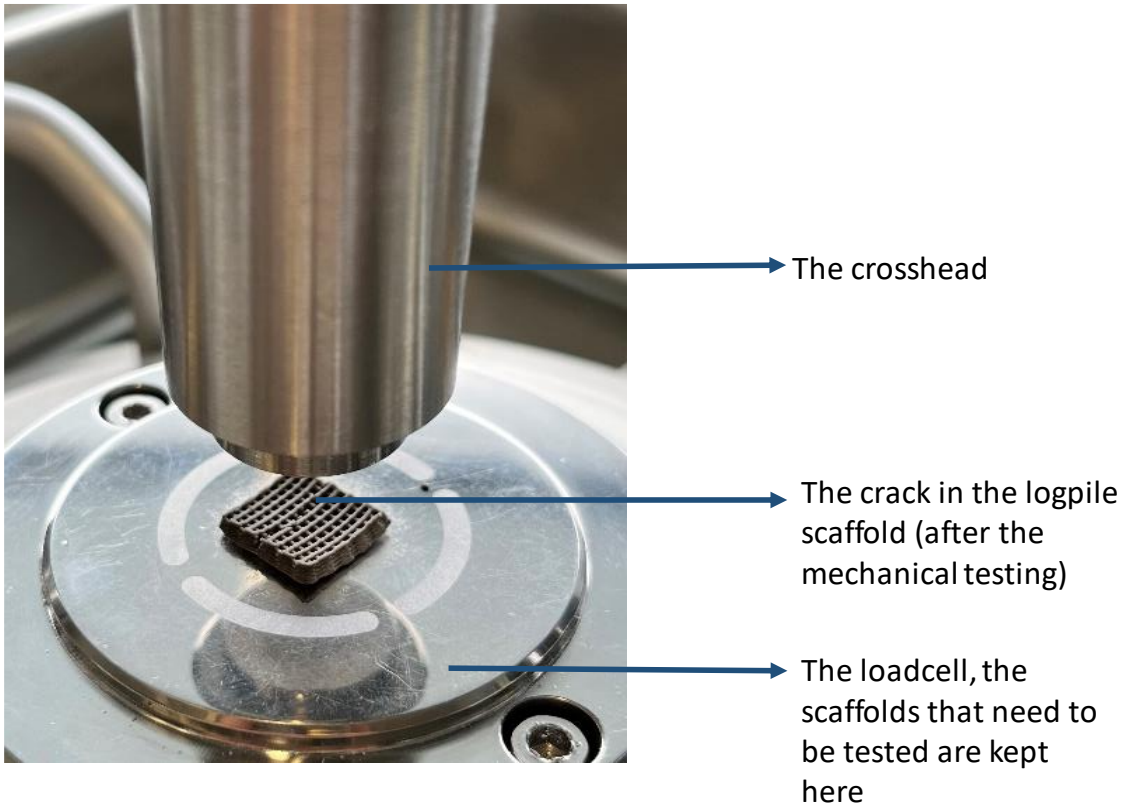

Figure 4 5. *Photograph of the broken logpile scaffold after the experiment*

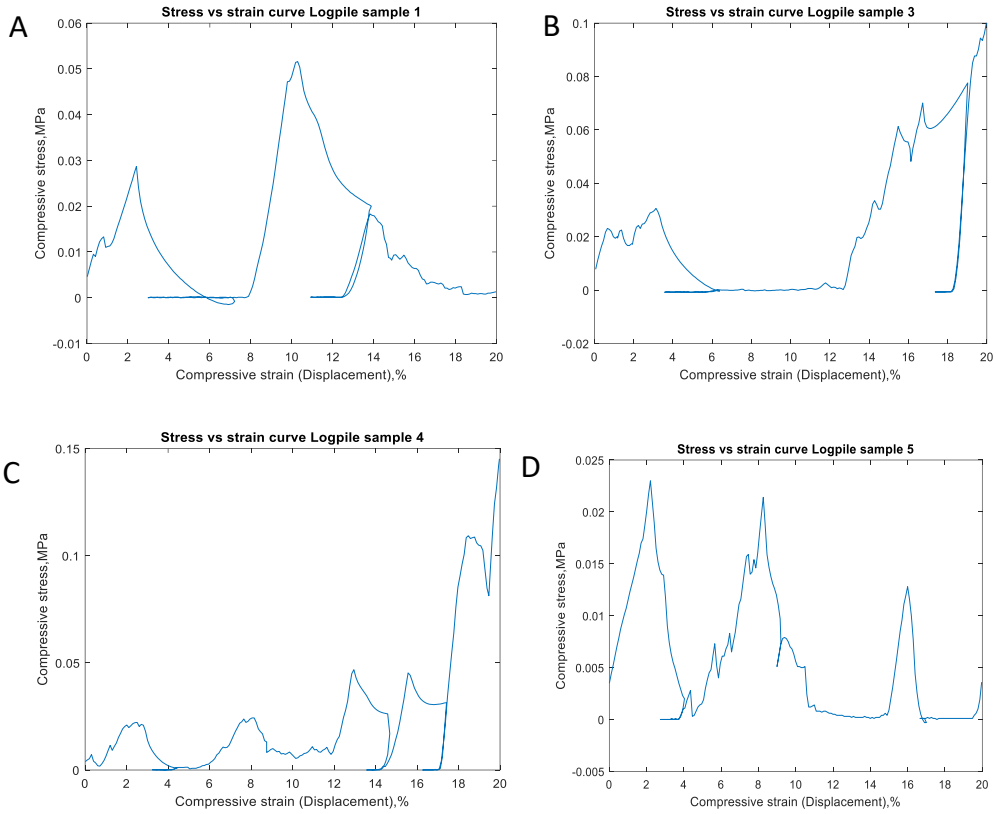

Figure 4 6. *The stress-strain curves of single logpile sample 2,3,4,5 that are shown as A, B, C, D respectively*

We also tested four more logpile samples that are shown in Figure 4.6. The abrupt reduction in compressive stress suggests a fracture that occurred during the trials. multiple periodic peaks indicate that the scaffolds have multiple fractures. Unlike the previous single hexagon scaffolds, for these logpile scaffolds, the mechanical testing did not stop before the compressive strain was 20% (as we selected in the Bluehill software). This was because these logpile scaffolds were not as severely broken as the hexagon ones. As a result, the test did not stop before 20%. The Young's modulus, first maximum compressive stress, maximum compressive stress before ultimate fracture and the compressive strain at the maximum compressive stress for the logpile scaffolds were calculated and stated in Table 4.4. The Young's modulus is essentially the slope of the figure's first

linear segment. The maximum compressive strength is the compressive stress that is achieved by the scaffolds just before the deformation.

Table 4.4. *Young's Modulus, maximum compressive strength and maximum compressive strain of the single logpile samples*

	Young's Modulus (MPa)	First Maximum Compressive Strength (MPa)	Maximum Compressive Strength before ultimate failure (MPa)	Maximum Compressive Strain (%)
Sample 1	0.7	0.01	0.009	1.8
Sample 2	1.4	0.03	0.054	2.4
Sample 3	2.6	0.02	0.1	0.7
Sample 4	2	0.02	0.14	2.5
Sample 5	0.7	0.02	0.022	2.2

4.5. Stress- strain curve of the stacked hexagon scaffold

We performed mechanical testing of the stacked hexagon samples (Figure 3.4) in the same manner that we did for the single hexagon and single logpile scaffold scaffolds. Figure 4.7 depicts the stress-strain curve for stacked hexagon scaffolds. The curve illustrates the behavior of stacked scaffolds under compressive load by plotting the amount of stress in MPa on the y-axis and the corresponding amount of strain in percentage on the x-axis. The applied force (N) is depicted on the right side of the y axis curve. The displacement values in millimeters are also displayed (see Figure 4.7).

In Figure 4.7, we see initially the compressive stress was increasing linearly until point (i), where the scaffold faced the first fracture. At point (i), the compressive stress was 1.85 MPa and the compressive strain was 1.9 %. The force at point (i) was 440 N. After point (i) the compressive stress was again increasing until point (ii), when it faced another fracture. However, from point (ii) to point (iii), the compressive stress and applied force were almost constant (4.5 MPa and 1079 N respectively). The compressive strain at point (ii) was 3.7% and at point (iii) was 4.8%. From point (ii) to point (iii) the compressive stress was constant because at this time the applied force was trying to bend the screws. We see after point (iii) there was a slight decrease in the value of compressive stress (4.5 MPa to 4.2 MPa) that means the screws were a little bent and the scaffolds faced a fracture. However, after point (iii) the compressive strength again started to increase until point (iv), when the screws were totally bent and the scaffold was almost fully broken

(see Figure 4.8). At this point (iv), the force value was 1558 N and the compressive stress was 6.5 MPa when the experiment ended.

In Figure 4.7, the stacked hexagon scaffold faced its first fracture at point (i) where the maximum compressive strength was 1.8 MPa and the compressive strain was 1.9%. We see the scaffold face periodic collapses at point (iii) and (iv). At point (iv), the scaffold achieved the maximum compressive strength before getting the ultimate fracture. At this point the compressive stress was 6.4 MPa and the force was 1453 N. Though we selected the strain as 20% in Bluehill software, the mechanical test was ended when the compressive strain was 7%. This was because, the stacked scaffolds were already severely broken before it reached the strain value 20%. So, the machine could not proceed the test farther. For similar reason, (see Figure 4.9) the sample A stopped at 14%, sample B at 8%, sample E at 6%.

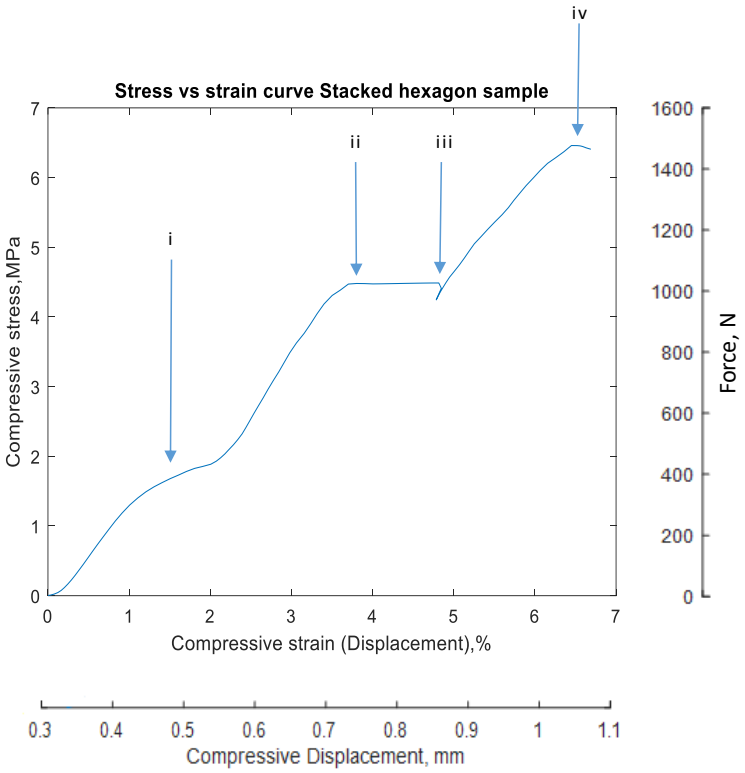

Figure 4 7. *Stress vs strain curve (and load displacement on second axes) for a representative stacked hexagon sample. The points labeled with Roman numerals represents the multiple collapses of the scaffold representative*

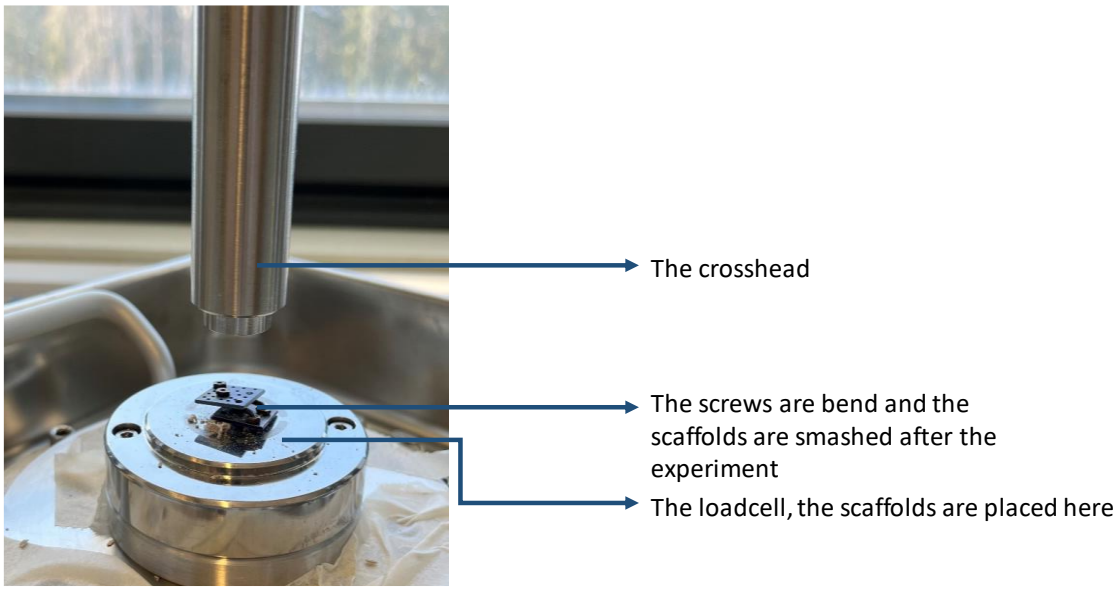

Figure 4 8. *Photograph of the broken stacked hexagon scaffold after the experiment*

We also tested four more stacked hexagon samples, which are depicted in Figure 4.9. The sudden decrease in compressive stress indicates a fracture that occurred during the testing. many periodic peaks imply many fractures in the scaffolds. The Young's modulus, first maximum compressive stress, maximum compressive stress before ultimate fracture and the compressive strain at the maximum compressive stress for the stacked hexagon samples were determined and reported in Table 4.5. The slope of the figure's first linear segment is effectively the Young's modulus. The maximum compressive

strength is the compressive stress attained by the scaffolds immediately prior to deformation.

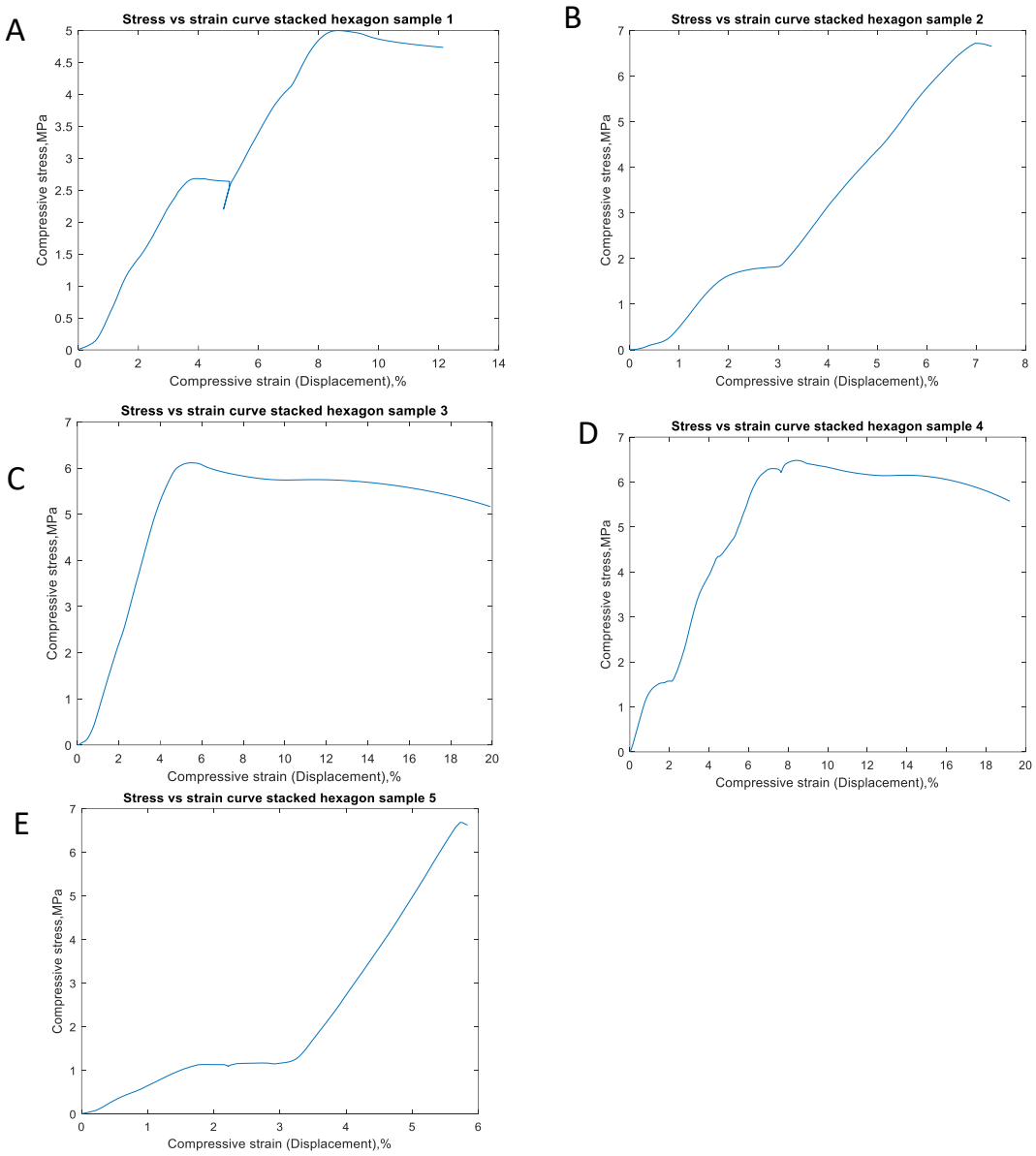

Figure 4 9. *The stress-strain curves of stacked hexagon sample 2,3,4,5,6 that are shown as A, B, C, D, E respectively*

Table 4.5. *Young's Modulus, maximum compressive strength and maximum compressive strain of the stacked hexagon samples*

	Young's Modulus (MPa)	First Maximum Compressive Strength (MPa)	Maximum Compressive Strength before ultimate failure (MPa)	Maximum Compressive Strain (%)
Sample 1	149.6	1.8	6.4	1.9
Sample 2	81	2.7	5	3.8
Sample 3	133.2	1.8	6.8	2.5
Sample 4	150.2	6.1	5.9	5.3
Sample 5	145.9	6.3	6.7	7.1
Sample 6	72	1.1	6.8	1.8

4.6. Stress- strain curve of the ordinary logpile scaffold

We also performed mechanical testing of the ordinary logpile samples (see Figure 1.1) that are typically used as bioactive glass scaffolds. The stress-strain curve of the sample is shown in Figure 4.10. The force (N) and displacement (mm) values are also shown in the curve. In Figure 4.10 we see that the curve was almost linear until the point (i) where the compressive stress was 2.8 MPa and the compressive strain was 0.9 %. The force at point (i) was 86.6 N and the displacement was 0.18 mm. Just after this point, the compressive stress drops a little bit that means the scaffold faced the first fracture. After that, the compressive stress was again increasing. However, at point (ii) and (iii), the scaffold experienced two major fractures where the compressive stress values were 9.3 MPa and 8 MPa respectively. The force values of these points were 289 N and 250 N respectively. After point (iii), the compressive stress decreased drastically and the experiment ended when the scaffolds was totally destroyed (see Figure 4.11).

So, the first maximum compressive strength was achieved at point (i) where the compressive strength value was 2.8 MPa. However, at point (ii), the scaffold experienced the maximum compressive strength before getting completely broken. At point (ii) the compressive strength was 9.3 MPa and the compressive strain was 2.5%. The force value was 289 N at this point. The test got ended when the compressive strain value was 20% (as we selected at the Bluehill software). In Figure 4.12 we see that, for sample A, the mechanical testing was ended at 18% as the sample was already destroyed by then. As

a result, the test could not proceed and got ended at 18%. However, for sample B, the test went all the way through 20% as the scaffold was not destroyed before that point.

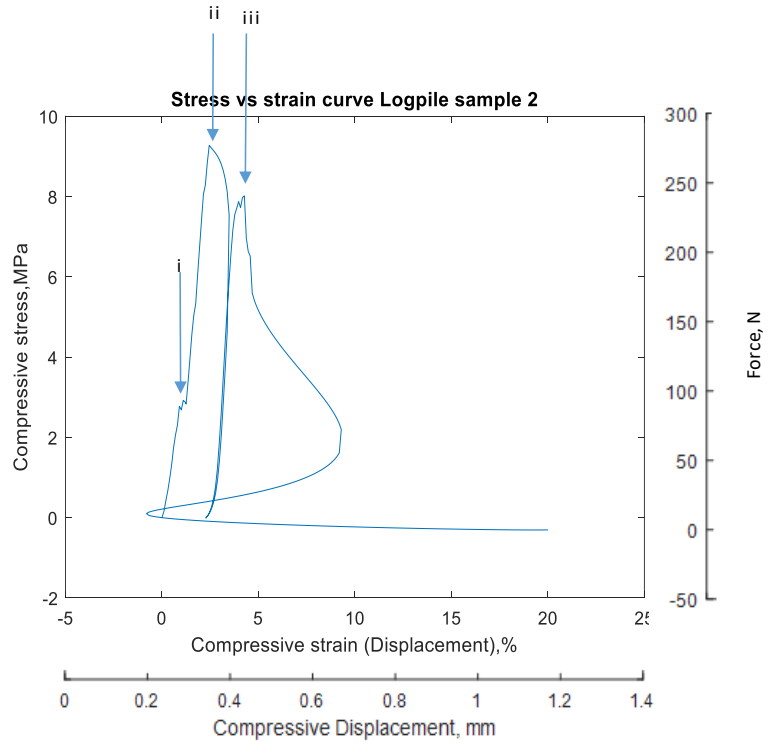

Figure 4 10. *Stress vs strain curve (and load displacement on second axes) for a representative ordinary logpile sample. The points labeled with Roman numerals represents the multiple collapses of the scaffold representative*

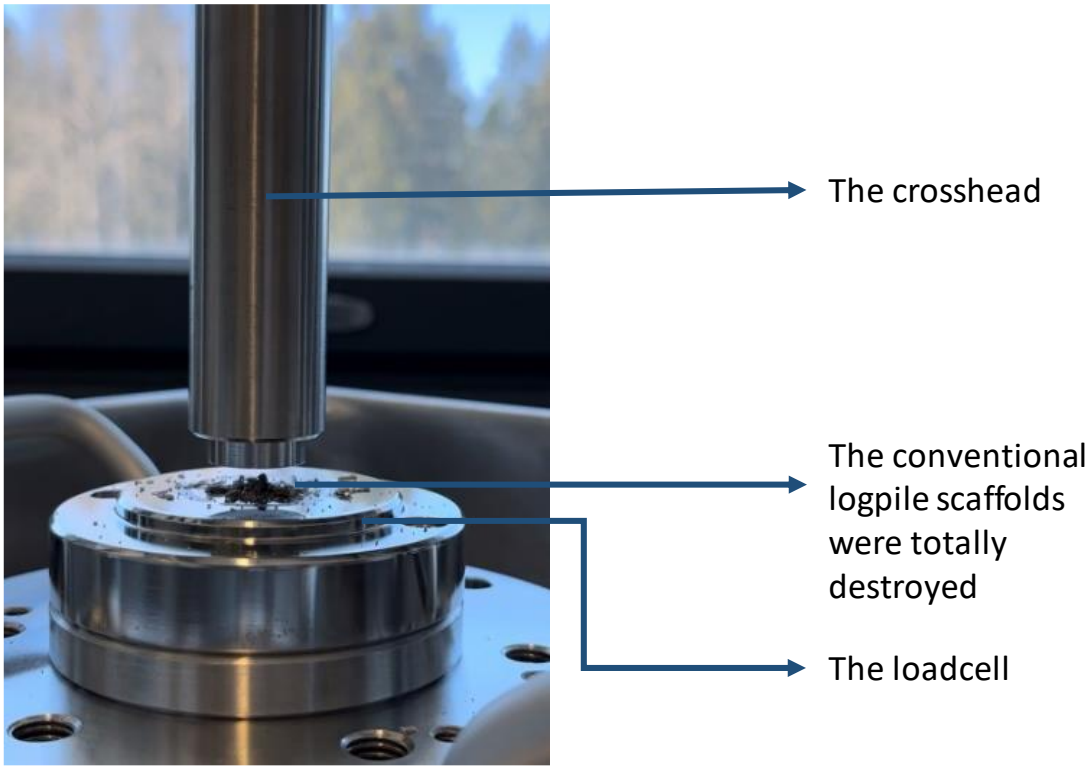

Figure 4 11. *Photograph of the broken ordinary logpile scaffold after the experiment*

We also tested two more ordinary logpile samples, which are depicted in Figure 4.12. The sudden decrease in compressive stress indicates a fracture that occurred during the testing. many periodic peaks imply many fractures in the scaffolds. The Young's modulus, first maximum compressive stress, maximum compressive stress before ultimate fracture and the compressive strain at the maximum compressive stress for the ordinary scaffolds were determined and reported in Table 4.6.

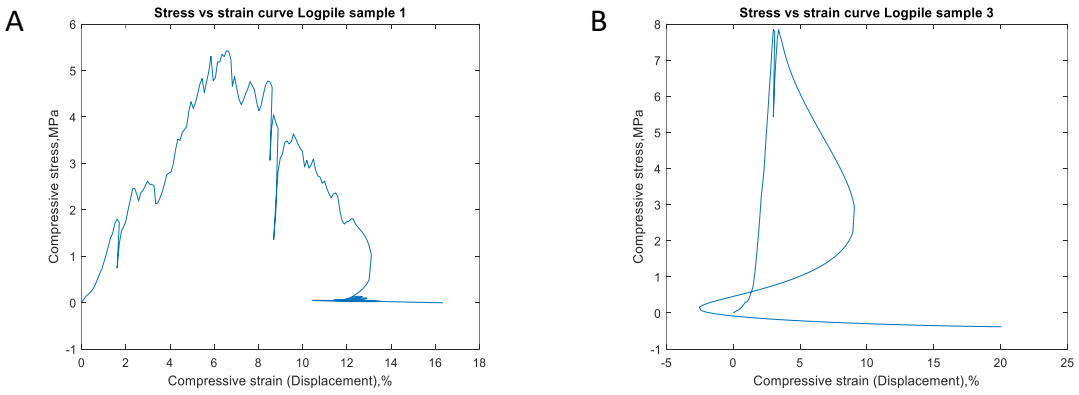

Figure 4 12. *The stress-strain curves of ordinary logpile sample 2 and 3 that are shown as A and B respectively*

Table 4.6. *Young's Modulus, maximum compressive strength and maximum compressive strain of the ordinary logpile samples*

	Young's Modulus (MPa)	First Maximum Compressive Strength (MPa)	Maximum Compressive Strength before ultimate failure (MPa)	Maximum Compressive Strain (%)
Sample 1	347.5 MPa	2.8 MPa	9.5	0.9
Sample 2	113.9	1.8	5.6	1.6
Sample 3	546	7.8	7.8	3

4.7. Comparing the results of the stacked hexagon to the single scaffolds and trabecular bone

We calculated the mean and standard deviations of the Young's modulus, maximum compressive strength and the Compressive Strain at Maximum Compressive Stress of the single hexagon, single logpile, the stacked hexagon scaffolds and the ordinary logpile scaffolds (from Table 4.3 to Table 4.6) in the Table 4.7.

In interpreting the data in Table 4.7, we will first compare the pure bioactive glass scaffolds with different geometries to each other, and then discuss the effect of the metal. Prior studies have found that with logpile scaffold geometries, most literature values for ultimate stress scale according to the Gibson-Ashby model between $(1\text{-}P)^{1.5}$ to $(1\text{-}P)^{2}$, where P is the porosity [62]; since 1-P was a third higher for the logpile specimens, if the geometry and sintering had no other effects we would expect the hexagons to have 50-70% higher ultimate stress than the logpiles, and 4-7 fold less than the ordinary logpile scaffolds. However, this relationship was not observed experimentally in Table 4.7. Although we did observe that the ordinary logpile scaffold was stronger than the single hexagonal scaffold, it was 24x stronger not 4-7. Moreover, the ordinary logpile scaffold was stronger than the logpile we made even though the ordinary one had a lower porosity. Indeed, the single logpile scaffolds were very fragile, getting their first fractures at as low as 1.9 N, while the ordinary logpiles was 86.6 N. The main difference between the ordinary logpiles and our logpile structures was the thickness of the struts (which affects the porosity) and the geometry. The logpile we made were much wider, and we observed significant warping at the corners after sintering. So, our logpile scaffolds were not 100% straight after sintering which affects the mechanical testing. While doing the mechanical testing of our logpile scaffolds, the contact area of the scaffolds was significantly low. As a result, they break at a very early point of the mechanical testing (see Table 4.7 where the maximum compressive strength is only 0.02 MPa which is extremely low). From the

values of Table 4.7, we see that, the Young's modulus, compressive strength and compressive strain at maximum compressive stress have increased largely for using the metal screws. The Young's modulus of the stacked hexagon scaffolds is almost 50 and 80 times of that of single hexagon and logpile scaffolds. However, if we compare these values with that of ordinary logpile scaffolds, the compressive strength of the single logpile scaffolds seems really low. While the ordinary scaffold's compressive strength is 3.3±2%, the single logpile scaffold has the compressive strength of only 0.02%.

Table 4.7 *Means and standard deviations of the maximum compressive stress, Young's modulus and compressive strain at maximum compressive stress of hexagon, logpile and stacked hexagon scaffolds and trabecular bone.*

	Single Hexagon Scaffolds	Single Logpile Scaffolds	ordinary logpile scaffolds	Stacked Hexagon Scaffolds	Trabecular bone
Young's Modulus (MPa)	2.4±1	1.5±0.7	329±216	122±33	50 to 500
Maximum Compressive Strength (MPa)	0.2±0.4	0.020±0.006	4.8±3	3.3±2	0.1–16
Compressive Strain at Maximum Compressive Stress (%)	0.9±0.8	1.9±0.7	1.8±0.8	3.7±1.9	

There are several factors that are responsible for this low compressive strength values. The logpile scaffolds that we were using were much larger than the ordinary ones. Because of being larger, they were not 100% straight after sintering. They were a little bit

concave (see figure 4.13). As a result, when we tested their mechanical properties, the contact area of the scaffolds with the piston was much lower than their original surface area. So the piston barely touches the logpile scaffolds and they got broken very easily. This is the probable reason that after the mechanical testing the logpile scaffolds just had couple of cracks (see Figure 4.5) while the ordinary scaffolds were totally destroyed (see Figure 4.11).

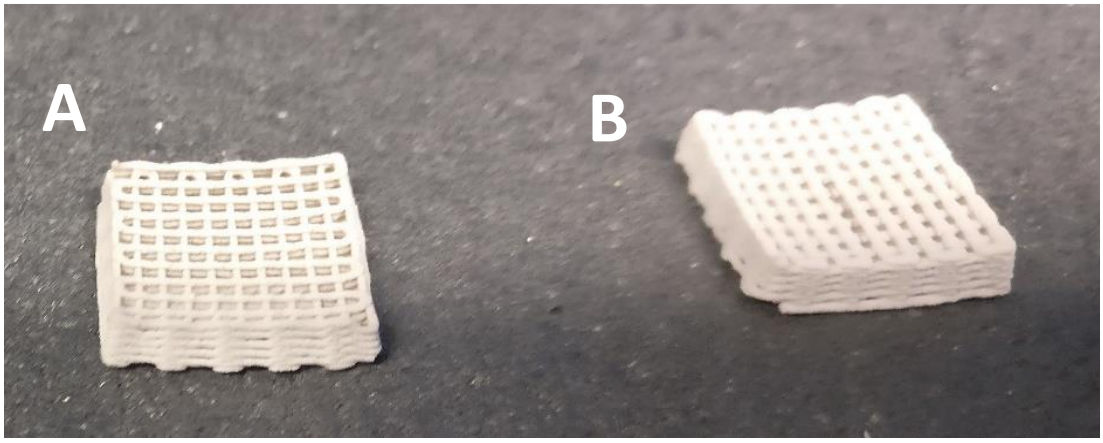

Figure 4 13. *Photograph of two single logpile scaffolds (The size for both of them was similar and it was around 12.5 mmx12.5 mmx 2.3 mm and weight were (A) 266 mg and (B) 294 mg). They were concave after being sintered.*

Another important factor is the porosity of the scaffolds. Generally, as the porosity of bioactive glass scaffolds increases, their compressive strength decreases. This is because higher porosity means there are more voids or empty spaces within the scaffold structure, which can lead to stress concentrations and make the scaffold more susceptible to failure under compressive loads [63]. The ordinary logpile scaffolds have the porosity of 43% where our logpile scaffolds have the porosity of 72.4%. So, the compressive strength is obviously lower for the bigger logpile scaffolds. The ordinary logpile scaffolds are much smaller than the logpile scaffolds that we tested. The smaller scaffolds are much more uniform and compact. So, they distribute loads better than the bigger logpile scaffolds that we used.

From Table 4.7, we see that the Young's modulus and maximum compressive strength of the stacked hexagon scaffolds are 122±33 MPa and 3.3±2 MPa that is almost 50 times and 16 times respectively increased than the single hexagon scaffolds. The stacked scaffolds have 100 times more compressive strength than the single logpile. So, the metal screws definitely added extra strength to the scaffolds. Moreover, the Young's Modulus and the maximum compressive strength value of the stacked hexagon samples

are within the range of Trabecular bone. Otherwise these parameters were way too low compared to the Trabecular bone.

So, larger scaffolds can be much weaker, and larger scaffolds are where the clinical problem is, and the metal screws mitigated this and allowed much larger strains than the ordinary scaffolds. Moreover, we expect it is controllable by the thickness and number of screws as well as how they lock with the plate. However, the main problem was the scaffolds bent after sintering which affect their mechanical properties. This opens up exciting possibility of separately optimizing biological properties of bioactive glass and mechanical properties of metal especially for large structures. Our stacked scaffolds were bigger and stackable but their mechanical properties were not as good as the ordinary logpile scaffolds. To improve their mechanical properties, the bending of the big scaffolds after sintering should be solved with future research.

Another important factor is maximum bite force. For an adult with healthy teeth, the maximum bite force is between 300 N to 600 N [64]. Here, the single hexagon and logpile scaffolds' maximum withstand able force was not more than 13 N which is extremely low. For the ordinary logpile scaffold it was 275 N. However, for the stacked hexagon it was 1453 N which was more than enough for the biting force. So, the maximum force value had shown quite promising result.

In future we can make the holes in the scaffolds larger so that thicker metal screws can be used to stack them. Thicker screws can provide better support to the scaffolds. In this thesis we stacked two scaffolds together. To have a better result, more scaffolds can be stacked so that they are stronger and have better mechanical support.

5. CONCLUSIONS

In recent years, the use of bioactive glass scaffolds shows great potential in the field of tissue engineering and regenerative medicine. These scaffolds possess unique properties that allow them to support cell attachment, proliferation, and differentiation, while also promoting the regeneration of damaged or diseased tissue. Additionally, the versatility of these scaffolds allows for their use in a wide range of applications, including dental and orthopedic implants, wound healing, and drug delivery. In this study, we tried to make large 3D printed scaffolds that have bigger holes and can be stacked with metal screws. The main intention of using the screws were to provide additional support to the scaffolds so that they have tunable compressive strength and modulus, at least close to the trabecular bones. The stacked hexagon bioactive scaffolds that we used in this study, had the maximum compressive strength and Young's Modulus in the range of trabecular bone. However, the ordinary logpile scaffolds have better results in terms of Young's Modulus and maximum compressive strength which was basically they have less porosity and small uniform size that help them to have good mechanical properties. However, the stacked scaffolds that we used in the studies, have larger porosity, bigger size and they are stackable with metal screws. These metal screws are made from stainless steel, which is widely used in orthopedic applications and does not produce an adverse reaction or toxicity when in contact with living tissue. So, we incorporate the bioactivity of the bioactive glass and the mechanical strength of the stainless steel screws.

Despite the promising results, further research is still needed to improve the results. Maybe we can make bigger pores where bigger screws can be stacked. The diameter of the metal screws that we used, was 1.5 mm which was small compared to the size of the titanium plates. The size of the titanium plates was 15mmx 15 mm, so the screw was relatively small to provide better support. So, thicker metal screws should be tried which can provide more support to the scaffolds. Another issue was we inserted four screws to stack the scaffolds with the titanium plates. If more screws were stacked, the scaffolds might get more support and might show better mechanical properties.

Another aspect was, we used B12.5 MgSr glass for printing the scaffolds because it does not get crystallized after sintering [57]. So, other bioactive glasses (such as: B25, B50, etc.) can also be tried and thus the results can be compared. Thus we might get some promising results from other bioactive glasses.

Moreover, further studies should be done to reduce the bending of the bigger scaffolds (after sintering) because this will definitely improve the mechanical properties of the scaffolds and make them desirable for specific tissue engineering applications.

One important advantage of our stacked hexagon scaffolds is they are modular. We can investigate the glass and the mechanical structure separately. We can also add other components to study and influence biochemistry. Moreover, the main advantage of being stacked is, the we do not need to 3D print one big scaffold. We can print in small parts and stack them together to construct the desired shape and size. The stacked scaffolds can withstand force up to 1453 N which is enough for biting which make them desirable while constructing a mandible. These potential benefits of these scaffolds make them a promising candidate for use in the development of regenerative therapies in future if proper research and development are done.

6. REFERENCES

[1] Mayfield CK, Ayad M, Lechtholz-Zey E, Chen Y, Lieberman JR. 3D-Printing for Critical Sized Bone Defects: Current Concepts and Future Directions. Bioengineering. 2022 Nov 11;9(11):680.Erasmus EP, Johnson OT, Sigalas I, Massera J. Effects of sintering temperature on crystallization and fabrication of porous bioactive glass scaffolds for bone regeneration. Scientific Reports. 2017 Jul 20;7(1):6046.

[2] Erasmus EP, Johnson OT, Sigalas I, Massera J. Effects of sintering temperature on crystallization and fabrication of porous bioactive glass scaffolds for bone regeneration. Scientific Reports. 2017 Jul 20;7(1):6046.

[3] Hutmacher DW. Scaffolds in tissue engineering bone and cartilage. Biomaterials. 2000 Dec 15;21(24):2529-43.

[4] Tomford WW. Transmission of disease through transplantation of musculoskeletal allografts. JBJS. 1995 Nov 1;77(11):1742-54.

[5] Bauer TW, Muschler GF. Bone graft materials: an overview of the basic science. Clinical Orthopaedics and Related Research®. 2000 Feb 1;371:10-27.

[6] El-Rashidy AA, Roether JA, Harhaus L, Kneser U, Boccaccini AR. Regenerating bone with bioactive glass scaffolds: A review of in vivo studies in bone defect models. Acta biomaterialia. 2017;62:1–28.

[7] Fu Q, Saiz E, Rahaman MN, Tomsia AP. Bioactive glass scaffolds for bone tissue engineering: state of the art and future perspectives. Materials Science and Engineering: C. 2011 Oct 10;31(7):1245-56.

[8] Fabert M, Ojha N, Erasmus E, Hannula M, Hokka M, Hyttinen J, Rocherullé J, Sigalas I, Massera J. Crystallization and sintering of borosilicate bioactive glasses for application in tissue engineering. Journal of materials chemistry B. 2017;5(23):4514-25.

[9] Roseti L, Parisi V, Petretta M, Cavallo C, Desando G, Bartolotti I, Grigolo B. Scaffolds for bone tissue engineering: state of the art and new perspectives. Materials Science and Engineering: C. 2017 Sep 1;78:1246-62.

[10] Meinel L, Hofmann S, Karageorgiou V, et al. Engineering cartilagelike tissue using human mesenchymal stem cells and silk protein scaffolds. Biotechnol Bioeng 2004;88:379–91.

[11] Sharma B, Elisseeff JH. Engineering structurally organized cartilage and bone tissues. Ann Biomed Eng 2004;32:148–59.

[12] Olivier V, Faucheux N, Hardouin P. Biomaterial challenges and approaches to stem cell use in bone reconstructive surgery. Drug Discov Today 2004;9:803–11.

[13] Salgado AJ, Coutinho OP, Reis RL. Bone tissue engineering: state of the art and future trends. Macromol Biosci 2004;4:743–65.

[14] Hench, L.L. The story of Bioglass®. J. Mater. Sci. Mater. Med. 2006, 17, 967-978.

[15] Thompson, I.D.; Hench, L.L. Mechanical properties of bioactive glasses, glass-ceramics and composites. Proc. Inst. Mech. Eng. Part H-J. Eng. Med. 1998, 212, 127-136.

[16] Boccaccini, A.R. Ceramics. In Biomaterials, artificial organs and tissue engineering, 1st ed.; Hench, L.L., Jones, J.R., Eds.; Woodhead Publishing Limited CRC Press: Cambridge, UK, 2005; Volume 1, pp. 26-36.

[17] Thompson, I.D. Biocomposites. In Biomaterials, Artificial Organs and Tissue Engineering, 1st ed.; Hench, L.L., Jones, J.R., Eds.; Woodhead Publishing Limited CRC Press: Cambridge, UK, 2005; Volume 1, pp. 48-58.

[18] Schieker M, Seitz H, Drosse I, Seitz S, Mutschler W. Biomaterials as scaffold for bone tissue engineering. European journal of trauma. 2006 Apr;32:114-24.

[19] Gerhardt LC, Boccaccini AR. Bioactive glass and glass-ceramic scaffolds for bone tissue engineering. Materials. 2010 Jul 6;3(7):3867-910.

[20] Olszta MJ, Cheng X, Jee SS, Kumar R, Kim YY, Kaufman MJ, Douglas EP, Gower LB. Bone structure and formation: A new perspective. Materials Science and Engineering: R: Reports. 2007 Nov 28;58(3-5):77-116.

[21] Hart NH, Nimphius S, Rantalainen T, Ireland A, Siafarikas A, Newton RU. Mechanical basis of bone strength: influence of bone material, bone structure and muscle action. Journal of musculoskeletal & neuronal interactions. 2017 Sep;17(3):114.

[22] Hadjidakis DJ, Androulakis II. Bone remodeling. Annals of the New York academy of sciences. 2006 Dec;1092(1):385-96.

[23] Parfitt AM. Bone remodeling, normal and abnormal: a biological basis for the understanding of cancer-related bone disease and its treatment. The Canadian journal of oncology. 1995 Dec 1;5:1-0.

[24] Cooper DM, Kawalilak CE, Harrison K, Johnston BD, Johnston JD. Cortical bone porosity: what is it, why is it important, and how can we detect it? Current osteoporosis reports. 2016 Oct;14:187-98.

[25] Ralston SH. Bone structure and metabolism. Medicine. 2013 Oct 1;41(10):581-5.

[26] Marcus R, Feldman D, Nelson DA, Rosen CJ. Osteoporosis: Two-Volume Set.

[27] Trippel SB. Primer on the Metabolic Bone Diseases and Disorders of Mineral Metabolism.

[28] Farbod K, Nejadnik MR, Jansen JA, Leeuwenburgh SC. Interactions between inorganic and organic phases in bone tissue as a source of inspiration for design of novel nanocomposites. Tissue Engineering Part B: Reviews. 2014 Apr 1;20(2):173-88.

[29] Feng X. Chemical and biochemical basis of cell-bone matrix interaction in health and disease. Current chemical biology. 2009 May 1;3(2):189-96.

[30] Marieb EN. Essentials of human anatomy & physiology. 9th - 10th International 2012. ed. San Francisco: Pearson/Benjamin Cummings; 2009.

[31] Rengachary SS. Bone morphogenetic proteins: basic concepts. Neurosurgical focus. 2002;13(6):e2.

[32] Sfeir C, Ho L, Doll BA, Azari K, Hollinger JO. Fracture Repair. 2005:21-44.

[33] Schmidt-Bleek K, Schell H, Lienau J, Schulz N, Hoff P, Pfaff M, et al. Initial immune reaction and angiogenesis in bone healing. Journal of tissue engineering and regenerative medicine; J Tissue Eng Regen Med. 2014;8(2):120-30.

[34] Frost HM. A 2003 update of bone physiology and Wolff's Law for clinicians. The Angle Orthodontist. 2004 Feb;74(1):3-15.

[35] Hogan L. Wolff's law: A way of understanding how bones change [Internet]. WebMD. WebMD; 2021 [cited 2023Mar15]. Available from: https://www.webmd.com/osteoporosis/what-is-wolffs-law

[36] Goodno BJ, Gere JM. Mechanics of materials. Cengage learning; 2020.

[37] Lin CY, Kang JH. Mechanical properties of compact bone defined by the stress-strain curve measured using uniaxial tensile test: a concise review and practical guide. Materials. 2021 Jul 28;14(15):4224.

[38] Rust Kr, Singleton Gt, Wilson J, Antonelli Pj. Bioglass Middle Ear Prosthesis : Long-Term Results. Am J Otol. 1996;17(3):371-4.

[39] Hench LL, Splinter RJ, Allen WC, Greenlee TK. Bonding mechanisms at the interface of ceramic prosthetic materials. Journal of biomedical materials research. 1971 Nov;5(6):117-41.

[40] Huang W, Day DE, Kittiratanapiboon K, Rahaman MN. Kinetics and mechanisms of the conversion of silicate (45S5), borate, and borosilicate glasses to hydroxyapatite in dilute phosphate solutions. Journal of Materials Science: Materials in Medicine. 2006 Jul;17:583-96.

[41] Rohanová D, Boccaccini AR, Yunos DM, Horkavcová D, Březovská I, Helebrant A. TRIS buffer in simulated body fluid distorts the assessment of glass–ceramic scaffold bioactivity. Acta biomaterialia. 2011 Jun 1;7(6):2623-30.

[42] Hench LL, Polak JM. Third-generation biomedical materials. Science. 2002 Feb 8;295(5557):1014-7.

[43] Rahaman MN, Day DE, Bal BS, Fu Q, Jung SB, Bonewald LF, Tomsia AP. Bioactive glass in tissue engineering. Acta biomaterialia. 2011 Jun 1;7(6):2355-73.

[44] Ducheyne P, Qiu Q. Bioactive ceramics: the effect of surface reactivity on bone formation and bone cell function. Biomaterials. 1999 Dec 1;20(23-24):2287-303.

[45] Wilson J, Pigott GH, Schoen FJ, Hench LL. Toxicology and biocompatibility of bioglasses. Journal of biomedical materials research. 1981 Nov;15(6):805-17.

[46] Lai W, Garino J, Ducheyne P. Silicon excretion from bioactive glass implanted in rabbit bone. Biomaterials. 2002 Jan 1;23(1):213-7.

[47] Chen QZ, Thompson ID, Boccaccini AR. 45S5 Bioglass®-derived glass–ceramic scaffolds for bone tissue engineering. Biomaterials. 2006 Apr 1;27(11):2414-25.

[48] Filho OP, La Torre GP, Hench LL. Effect of crystallization on apatite-layer formation of bioactive glass 45S5. Journal of Biomedical Materials Research: An Official Journal of The Society for Biomaterials and The Japanese Society for Biomaterials. 1996 Apr;30(4):509-14.

[49] Yao A, Wang D, Huang W, Fu Q, Rahaman MN, Day DE. In vitro bioactive characteristics of borate-based glasses with controllable degradation behavior. Journal of the American Ceramic Society. 2007 Jan;90(1):303-6.

[50] Fu Q, Rahaman MN, Fu H, Liu X. Silicate, borosilicate, and borate bioactive glass scaffolds with controllable degradation rate for bone tissue engineering applications. I. Preparation and in vitro degradation. Journal of biomedical materials research part A. 2010 Oct;95(1):164-71.

[51] Fu Q, Saiz E, Rahaman MN, Tomsia AP. Bioactive glass scaffolds for bone tissue engineering: state of the art and future perspectives. Materials Science and Engineering: C. 2011 Oct 10;31(7):1245-56.

[52] Jones JR. Review of bioactive glass: from Hench to hybrids. Acta biomaterialia. 2013 Jan 1;9(1):4457-86.

[53] Rahaman MN, Day DE, Bal BS, Fu Q, Jung SB, Bonewald LF, Tomsia AP. Bioactive glass in tissue engineering. Acta biomaterialia. 2011 Jun 1;7(6):2355-73.

[54] Skallevold HE, Rokaya D, Khurshid Z, Zafar MS. Bioactive glass applications in dentistry. International Journal of Molecular Sciences. 2019 Nov 27;20(23):5960.

[55] Cannio M, Bellucci D, Roether JA, Boccaccini DN, Cannillo V. Bioactive glass applications: A literature review of human clinical trials. Materials. 2021 Sep 20;14(18):5440.

[56] Gorustovich AA, López JM, Guglielmotti MB, Cabrini RL. Biological performance of boron-modified bioactive glass particles implanted in rat tibia bone marrow. Biomedical Materials. 2006 Jun 5;1(3):100.

[57] Szczodra A, Tainio JM, Houaoui A, Liu H, Pohjola J, Miettinen S, Brauer DS, Massera J. Impact of borosilicate bioactive glass scaffold processing and reactivity on in-vitro dissolution properties. Materials Today Communications. 2023 Apr 11:105984.

[58] Uhlířová T, Pabst W. Conductivity and Young's modulus of porous metamaterials based on Gibson-Ashby cells. Scripta Materialia. 2019 Jan 15;159:1-4.

[59] Lutzweiler G, Ndreu Halili A, Engin Vrana N. The overview of porous, bioactive scaffolds as instructive biomaterials for tissue regeneration and their clinical translation. Pharmaceutics. 2020 Jun 29;12(7):602.

[60] Karageorgiou V, Kaplan D. Porosity of 3D biomaterial scaffolds and osteogenesis. Biomaterials. 2005 Sep 1;26(27):5474-91.

[61] Shimko DA, Shimko VF, Sander EA, Dickson KF, Nauman EA. Effect of porosity on the fluid flow characteristics and mechanical properties of tantalum scaffolds. Journal of Biomedical Materials Research Part B: Applied Biomaterials: An Official Journal of The Society for Biomaterials, The Japanese Society for Biomaterials, and The Australian Society for Biomaterials and the Korean Society for Biomaterials. 2005 May;73(2):315-24.

[62] Danilevicius P, Georgiadi L, Pateman CJ, Claeyssens F, Chatzinikolaidou M, Farsari M. The effect of porosity on cell ingrowth into accurately defined, laser-made, polylactide-based 3D scaffolds. Applied Surface Science. 2015 May 1;336:2-10.

[63] Liu Q, Lu WF, Zhai W. Toward stronger robocast calcium phosphate scaffolds for bone tissue engineering: A mini-review and meta-analysis. Biomaterials Advances. 2022 Mar 1;134:112578.

[64] Bakke M. Bite force and occlusion. InSeminars in orthodontics 2006 Jun 1 (Vol. 12, No. 2, pp. 120-126). WB Saunders.

7. APPENDICES

The 3D printer moves the sample stage to a series of positions while the ink is continuously extruded from the nozzle. The program loads the positions sequentially (each line) from a text document. For example, the command “move 1 2 3” will move the stage by 1 mm in x, 2 mm in y, and the nozzle by 3 mm in z. To generate logpiles, the stage typically, one moves the stage in a serpentine pattern horizontally, then rises by 0.3 mm, and then moves in a serpentine pattern vertically, and repeats. The hexagonal patterns involve many more steps, and become prohibitive to code by hand. Thus, we developed MATLAB scripts to automatically write text files according to set parameters to give specific lengths, heights, widths and line spacing. Appendix A is the code for the hexagonal scaffolds, and Appendix B is the code for the logpile scaffolds.

Appendix A: MATLAB code for printing Hexagon scaffolds

```
function [M2,Pos2]=Hexa_c(M2,Pos2,h_steps2,v_steps2,levels2, h_2, v_2,r,k,
z_length2)
%This function sets default variables if values are not entered


if nargin<10 %if the number of argument of the function is less than 10
    z_length2=0.3;    %the height of each layer
end
if nargin<9
    k=0.41;             %The displacement of the tip of the hexagon
end
if nargin==6
    v_2=round(100*h_2*0.525/0.909)/100;        % rounding the values so that the scaf-
folds do not get skewed
    r=round(100*h_2*1.05/0.909)/100;           % rounding the values so that the scaf-
folds do not get skewed


end
if nargin<6
    h_2=0.91; v_2=0.53; r=1.05; k=0.41;          %generating hexagon shape for each
layer going up
end
if nargin<5
    levels2=8;
end
if nargin<4
    v_steps2=9;
end
if nargin<3
    h_steps2=4;
end
if nargin<2
    M2=[0 0 0];
end

if (M2==[0 0 0])   %Generating from scratch, initialize print by moving nozel in L shape
    Pos2(1,:)=[-10 -10 0];
    M2(1,:)=[10 0 0];
    Pos2=[Pos2; Pos2(end,:)+M2(end,:)];
    M2(2,:)=[0 10 0];
    Pos2=[Pos2; Pos2(end,:)+M2(end,:)];
end
%----------------finished initializing/setting defaults----------------


for l=1:levels2 % for each layer
    fprintf('Level %i \n', l);
    if mod(l,2)==1 %Odd level
        for vs=1:v_steps2   %vs is vertical step number
            if mod(vs,2)==1 % Way up
                for hs=1:h_steps2   %hs is horizontal step number
```

```
                if hs==h_steps2 %last horizontal step
                    M2=[M2;[k/2+h_2 v_2 0]];      Pos2=[Pos2; Pos2(end,:)+M2(end,:)];


                    if vs==v_steps2, %if last step on level, go up one level
                        M2=[M2; [0 0 z_length2]]; Pos2=[Pos2; Pos2(end,:)+M2(end,:)];
                    end

                else
                    M2=[M2;[h_2 v_2 0]];     Pos2=[Pos2; Pos2(end,:)+M2(end,:)];
                    M2=[M2;[0 r 0]];         Pos2=[Pos2; Pos2(end,:)+M2(end,:)];
                    M2=[M2;[-h_2 v_2 0]];    Pos2=[Pos2; Pos2(end,:)+M2(end,:)];
                    M2=[M2;[0 r 0]];         Pos2=[Pos2; Pos2(end,:)+M2(end,:)];
                end
            end
        else  %even vs =>Way down
            for hs=1:h_steps2   %hs is horizontal step number
                if hs==h_steps2 %last horizontal step
                    M2=[M2;[k/2+h_2 -v_2 0]];      Pos2=[Pos2; Pos2(end,:)+M2(end,:)];

                    if vs==v_steps2, %if last step on level, go up one level

                        M2=[M2; [0 0 z_length2]]; Pos2=[Pos2; Pos2(end,:)+M2(end,:)];
                    end

                else
                    M2=[M2;[h_2 -v_2 0]];     Pos2=[Pos2; Pos2(end,:)+M2(end,:)];
                    M2=[M2;[0 -r 0]];         Pos2=[Pos2; Pos2(end,:)+M2(end,:)];
                    M2=[M2;[-h_2 -v_2 0]];    Pos2=[Pos2; Pos2(end,:)+M2(end,:)];
                    M2=[M2;[0 -r 0]];         Pos2=[Pos2; Pos2(end,:)+M2(end,:)];
                end
            end
        end %way down
    end
    elseif mod(l,2)==0  %Even Level

    for vs=1:v_steps2
        if mod(vs,2)==1 % Way towards left
            for hs=1:h_steps2
                if hs==h_steps2 %last vertical step
                    M2=[M2;[-v_2 -(k/2+h_2) 0]];      Pos2=[Pos2; Pos2(end,:)+M2(end,:)];


                    if vs==v_steps2, %if last step on level, go up one level
                        M2=[M2;[-Pos2(end,1) -Pos2(end,2) 0]]; Pos2=[Pos2;
Pos2(end,:)+M2(end,:)];
                        M2=[M2; [0 0 z_length2]];     Pos2=[Pos2; Pos2(end,:)+M2(end,:)];
                    end

                else
                    M2=[M2;[-v_2 -h_2 0]];           Pos2=[Pos2; Pos2(end,:)+M2(end,:)];
                    M2=[M2;[-r 0 0]];                Pos2=[Pos2; Pos2(end,:)+M2(end,:)];
                    M2=[M2;[-v_2 h_2 0]];            Pos2=[Pos2; Pos2(end,:)+M2(end,:)];
                    M2=[M2;[-r 0 0]];                Pos2=[Pos2; Pos2(end,:)+M2(end,:)];
                end
```

```
            end

        else  %even vs =>Way to right
            for hs=1:h_steps2
                if hs==h_steps2    %last vertical step
                    M2=[M2;[v_2 -(k/2+h_2) 0]];      Pos2=[Pos2; Pos2(end,:)+M2(end,:)];

                    if vs==v_steps2, %if last step on level, go up one level

                        M2=[M2; [0 0 z_length2]];    Pos2=[Pos2; Pos2(end,:)+M2(end,:)];
                    end

                else
                    M2=[M2;[v_2 -h_2 0]];          Pos2=[Pos2; Pos2(end,:)+M2(end,:)];
                    M2=[M2;[r 0 0]];              Pos2=[Pos2; Pos2(end,:)+M2(end,:)];
                    M2=[M2;[v_2 h_2 0]];          Pos2=[Pos2; Pos2(end,:)+M2(end,:)];
                    M2=[M2;[r 0 0]];              Pos2=[Pos2; Pos2(end,:)+M2(end,:)];
                end
            end
        end
    end


    end


end
figure; plot(Pos2(:,1),Pos2(:,2));
axis('equal');


%Saving the values in a text file so that it can be used as a printing script
fileID = fopen(uiputfile('*.txt'), 'w');   % "fopen(... 'a') means append to end of file, while
'w' means overwrite.
fprintf (fileID, 'speed 4\n')  %Print the printing speed
for i=1:size(M2,1)

    fprintf(fileID, 'move %.1f %.1f %.1f\n',M2(i,1), M2(i,2), M2(i,3));  % Print the values in
3 columns which is required as a script of 3D printing

end
fclose(fileID);
```

Appendix B: MATLAB code for printing Logpile scaffolds

```
function [M,Pos]=logpile(M,Pos,h_length,h_steps,v_length,v_steps,levels,z_length)
%This function sets default variables if values are not entered


if nargin<8
    z_length=0.3;   %the height of each layer
end
if nargin<7
    levels=4; % the number of layers
end
if nargin<3
    h_length=7.2; h_steps=5; v_length=0.72; v_steps=5;
end
if nargin<2 | M==[0 0 0] % initializing the matrix
    Pos(1,:)=[-10 -10 0];
    M(1,:)=[10 0 0];
    Pos=[Pos; Pos(end,:)+M(end,:)];
    M(2,:)=[0 10 0];
    Pos=[Pos; Pos(end,:)+M(end,:)];
end

M=[M;[0 0 z_length]];    Pos=[Pos; Pos(end,:)+M(end,:)];  %Going to next layer after
ptinting each layer


for j=1:levels  % Each layer of the logpile sample
  if mod(j,2)==1 %odd level

    for i=1:h_steps
        if i==h_steps
            M=[M;[h_length 0 0]];     Pos=[Pos; Pos(end,:)+M(end,:)];
            M=[M;[0 v_length 0]];     Pos=[Pos; Pos(end,:)+M(end,:)];
            M=[M;[-h_length 0 0]];    Pos=[Pos; Pos(end,:)+M(end,:)];
            M=[M;[0 v_length 0]];     Pos=[Pos; Pos(end,:)+M(end,:)];
            M=[M;[h_length 0 0]];     Pos=[Pos; Pos(end,:)+M(end,:)];
        else
            M=[M;[h_length 0 0]];     Pos=[Pos; Pos(end,:)+M(end,:)];
            M=[M;[0 v_length 0]];     Pos=[Pos; Pos(end,:)+M(end,:)];
            M=[M;[-h_length 0 0]];    Pos=[Pos; Pos(end,:)+M(end,:)];
            M=[M;[0 v_length 0]];     Pos=[Pos; Pos(end,:)+M(end,:)];
        end

    end
          M=[M;[0 0 z_length]];    Pos=[Pos; Pos(end,:)+M(end,:)];
elseif mod(j,2)==0 %even level
    for i=1:v_steps
        if i==v_steps
            M=[M;[0 -h_length 0]];     Pos=[Pos; Pos(end,:)+M(end,:)];
            M=[M;[-v_length 0 0]];     Pos=[Pos; Pos(end,:)+M(end,:)];
            M=[M;[0 h_length 0]];      Pos=[Pos; Pos(end,:)+M(end,:)];
```

```
            M=[M;[-v_length 0 0]];     Pos=[Pos; Pos(end,:)+M(end,:)];
            M=[M;[0 -h_length 0]];     Pos=[Pos; Pos(end,:)+M(end,:)];

        else
            M=[M;[0 -h_length 0]];     Pos=[Pos; Pos(end,:)+M(end,:)];
            M=[M;[-v_length 0 0]];     Pos=[Pos; Pos(end,:)+M(end,:)];
            M=[M;[0 h_length 0]];      Pos=[Pos; Pos(end,:)+M(end,:)];
            M=[M;[-v_length 0 0]];     Pos=[Pos; Pos(end,:)+M(end,:)];
        end

    end
   M=[M;[0 0 z_length]];    Pos=[Pos; Pos(end,:)+M(end,:)];
end

end

figure; plot(Pos(:,1),Pos(:,2));
axis('equal');



%Saving the values in a text file so that it can be used as a printing script
fileID = fopen(uiputfile('*.txt'), 'w');   % "fopen(... 'a') means append to end of file, while
'w' means overwrite.
fprintf (fileID, 'speed 4\n')  %Print the printing speed
for i=1:size(M,1)

    fprintf(fileID, 'move %.1f %.1f %.1f\n',M(i,1), M(i,2), M(i,3)); % Print the values in 3
columns which is required as a script of 3D printing
end
fclose(fileID);
```